Efficient assessment of combined crystallization, milling, and dissolution cycles for crystal size and shape manipulation

Author(s):
Salvatori, Fabio; Binel, Pietro; Mazzotti, Marco

Publication Date:
2019-02

Permanent Link:

https://doi.org/10.3929/ethz-b-000328397 →

Originally published in:

Chemical Engineering Science: X 1, http://doi.org/10.1016/j.cesx.2018.100004 →

Chemical Engineering Science: X 1 (2019) 100004

Contents lists available at ScienceDirect

Chemical Engineering Science: X

journal homepage: www.elsevier.com/locate/cesx

Efficient assessment of combined crystallization, milling, and dissolution cycles for crystal size and shape manipulation

Fabio Salvatori, Pietro Binel, Marco Mazzotti *

Institute of Process Engineering, ETH Zurich, 8092 Zurich, Switzerland

ARTICLE INFO

Article history:
Received 16 October 2018
Received in revised form 4 December 2018
Accepted 23 December 2018

Keywords:
Population balance equation
Crystallization
Process characterization
Process modeling
Particle morphology
Process design

ABSTRACT

A 3-stage process, consisting of a combination of crystallization, milling, and dissolution stages for the selective manipulation of the size and shape of crystals, is investigated to characterize its performance when applied to different substances. To this aim, simulations are used to screen, via a parametric analysis, the effect of different compound properties and operating conditions on the size and shape of the final products. Through this analysis, characteristic trends of general validity are identified, thus allowing to define families of compounds with similar behavior and features. Based on these results, a set consisting of a small number of experiments is devised to fully characterize the outcome of the 3-stage process for a specific substance. An experimental validation is carried out by performing this set of experiments with two compounds, namely β L-Glutamic acid and γ D-Mannitol, thus assessing the suitability of this method for a comprehensive characterization of the process and its outcome. The information collected at the end of the different stages throughout all the experiments is further exploited to estimate the growth rates of γ D-Mannitol, in order to validate the observations made through simulations regarding the effect of growth kinetics on the process outcome. Finally, the model, fitted to the experimental evidence collected, has been used to further investigate and characterize the design space.

1. Introduction

Crystallization is one of the most used separation and purification processes in the pharmaceutical and food industry. The properties of the crystals, such as their polymorphism and their morphology, are important both for their behavior in the downstream processes (Gordon, 1994; Sun and Grant, 2001; Nokhodchi et al., 2010; Sun, 2011; Chatterjee et al., 2017) and for the quality of the final commercialized products (Liversidge and Cundy, 1995; Chemburkar, 2000; Singhal and Curatolo, 2004; Bakalis et al., 2011; Khadka et al., 2014). In particular, the size and the shape of the crystals are known to significantly impact the performance of steps as filtration and tableting, thus rising interest in developing methods to directly manipulate the particle morphology at the crystallization stage. Currently, two are the major alternatives available. The first involves the use of additives, to modify how the solute molecules are integrated onto specific crystal facets (Shangwal, 2007; Klapwijk et al., 2016; Simone et al., 2015). Numerous studies have proven how the same compound can exhibit significantly different morphologies depending on the type of additive used and on its amount (van Antwerpen and van Krevelen, 1972; Salvalaglio et al., 2013; Powell et al., 2016; Simone et al., 2017; Taborga et al., 2017). However, the additives that can be exploited in pharmaceutical processes are regulated and strongly limited by their impact on human health, thus restricting the possibility of effectively manipulating crystal morphology and their application in industrial processes. Therefore, the most widespread industrial technique exploited to manipulate crystal habit is milling. Here, mechanical force is applied to break the individual crystals and to obtain more equantly shaped particles. However, the high stresses induced by the forces applied and the strong temperature increment experienced by the solid particles may lead to undesired solid-state transformations (Gupta et al., 2003; Heng et al., 2006; Lin et al., 2010), which would alter the properties of the final product. Furthermore, the large amount of fines formed during breakage represents a problem during filtration (Tien et al., 1996), leading to long process times with a higher risk of product decomposition.

In previous publications (Salvatori and Mazzotti, 2017, 2018a) we have investigated the possibility of combining crystallization, milling, and dissolution stages into a new process, called 3-stage process, to selectively manipulate the size and shape of crystals while mitigating the drawbacks characteristic of each unit operation. The strategy underlying the new technology is to let crystals grow under typical crystallization conditions and to subsequently

* Corresponding author.
E-mail address: marco.mazzotti@ipe.mavt.ethz.ch (M. Mazzotti).

https://doi.org/10.1016/j.cesx.2018.100004
2590-1400/

Nomenclature

B	birth term in the PBE [$\mu m^{-2}\ kg^{-1}\ s^{-1}$]
c	solute concentration in the liquid phase [$g\ kg^{-1}$]
c_0	initial solute concentration in the liquid phase [$g\ kg^{-1}$]
c^*	solubility [$g\ kg^{-1}$]
C_j	confidence interval for the j-th parameter [varies]
D_i	dissolution rate for dimension i [$\mu m\ s^{-1}$]
E	death term in the PBE [$\mu m^{-2}\ kg^{-1}\ s^{-1}$]
F	objective function [–]
g_i	daughter distribution of the fragments along the i-th dimension [μm^{-1}]
$\mathbf{G}$	vector of rates of change [$\mu m\ s^{-1}$]
G_i	growth rate for dimension i [$\mu m\ s^{-1}$]
$\boldsymbol{J}$	jacobian of the model [varies]
J_N	nucleation rate [$kg^{-1}\ s^{-1}$]
J_S	secondary nucleation rate [$kg^{-1}\ s^{-1}$]
J_{He}	heterogeneous primary nucleation rate [$kg^{-1}\ s^{-1}$]
J_{Ho}	homogeneous primary nucleation rate [$kg^{-1}\ s^{-1}$]
$\mathbf{k}_D$	vector of dissolution rate parameters [varies]
$\mathbf{k}_G$	vector of growth rate parameters [varies]
$\mathbf{k}_{Hom}$	vector of homogeneous nucleation rate parameters [varies]
$\mathbf{k}_{Het}$	vector of heterogeneous nucleation rate parameters [varies]
$\mathbf{K}_i$	vector of breakage frequency parameters [varies]
k_v	shape factor [–]
K_i	breakage frequency for dimension i [s^{-1}]
L_i	crystals characteristic dimension i [μm]
$L_{i,N}$	number-weighted average characteristic dimension i [μm]
$L_{i,V}$	volume-weighted average characteristic dimension i [μm]
m_0	mass of seeds per kg of solvents [g/kg]
m_D	percentage of mass dissolved [–]
m_M	mass of the rotor [g]
m_S	suspension density [$g\ kg_S^{-1}$]
n	number density function [$\mu m^{-2}\ kg^{-1}$]
n_0	PSD of seed crystals [$\mu m^{-2}\ kg^{-1}$]
n_C	number of process cycles [–]
N_E	total number of experimental observations [–]
N_O	number of considered outputs [–]
N_P	power number [–]
$\mathbf{p}$	vector of estimated growth rate parameters [varies]
S	supersaturation [–]
$\boldsymbol{S}$	covariance matrix [varies]
t	time [s]
T	temperature [°C]
$T_{0,C1}$	initial process temperature [°C]
$T_{f,Cn}$	final process temperature [°C]
$\boldsymbol{V}$	positive semidefinite covariance matrix [varies]
x	size of the mother particle during a breakage event [μm]
w_{ij}	weights in the objective function [–]
y_i	characteristic property of the measured particle size and shape distribution for the i-th experiment [μm]
Γ	growth/dissolution rate [$\mu m\ s^{-1}$]
γ_C	cooling rate [$°C\ min^{-1}$]
γ_D	heating rate [$°C\ min^{-1}$]
ε	power input [$W\ kg^{-1}$]
Φ	aspect ratio [–]
μ_{ij}	cross moment ij of the PSSD [varies]
ρ	density of the crystalline phase [$kg\ m^{-3}$]
$\sigma_{1,N}$	number-weighted standard deviation in L_1 direction [μm]
$\sigma_{2,N}$	number-weighted standard deviation in L_2 direction [μm]
τ	residence time in the mill [s]
θ	rotor speed [rpm]

mill them, breaking them mainly along their shorter dimension, thus producing more compact crystals. The fine particles formed are then dissolved and the excess of solute in the liquid phase is recovered by repeating these three steps cyclically. A first assessment of the process analyzing the qualitative trends in terms of average sizes and dispersity of the distribution was carried out by performing an in silico investigation (Salvatori and Mazzotti, 2017). The mathematical model used to carry out the study was structured so as to specifically describe the phenomena occurring during each stage, but it was not fitted to a specific substance, in order to keep the observation as generally valid as possible. The effect of a subset of the most important operating conditions was thoroughly analyzed and some heuristic optimum conditions were identified. More recently, a comprehensive set of experiments has been performed to assess the results of the simulations and to verify the possibility of effectively tuning particle morphology in practice (Salvatori and Mazzotti, 2018a). The results highlighted how the process, when applied to β L-Glutamic acid, can effectively produce particles satisfying the product specifications, thus yielding product particles with a quality superior to that of the crystals obtained via more conventional processes. However, the study has also highlighted how the productivity of the 3-stage process is significantly lower than that of the other processes analyzed for comparison. Furthermore, process characterization requires a large effort when it comes to estimating the set of process outcome for different, newly explored compounds.

Despite being aware of the great potential of the 3-stage process in changing particle size and shape, we are also aware of its shortcomings, especially concerning its implementation to compounds with very different properties, its time consuming characterization, and its reduced productivity. Therefore, in this work, we aim at specifically tackling these problems, by providing a shortcut method with a reduced characterization effort, to assess the potential and feasibility of the 3-stage process when applied to new systems. To do so, we apply the methodology developed in the previous publications, both for simulations and experiments, extending it to the whole range of operating conditions that can be effectively applied, using the available experimental setup. Both a new set of simulations and a new set of experiments, involving also a new compound for which no information on the characteristic growth or dissolution kinetics is readily available, are performed; we analyze and exploit the results from a completely new perspective. The paper is structured as follows. In Section 2 the mathematical model is presented, along with the fitting procedure for parameter estimation, the method adopted to identify the required set of experiments, and the theoretical evidence at the basis of the proposed approach. In Section 3, the model compounds and the experimental setup are described and the procedure to perform the laboratory tests is reported in detail. In Section 4 the experimental evidence is reported, analyzed, and discussed, focusing on the quantity and type of information that can be collected throughout the experimental campaign and how it can be exploited during the process design stage. Finally, Section 5 draws conclusions.

2. Theory, modeling, and simulation results

The aim of this work is to develop a robust and effective strategy to investigate the 3-stage process and to understand under

which conditions it should be operated for the specific system considered. In this section, the theoretical basis of the approach developed and proposed is presented; the results of such in silico analysis will guide the experimental assessment. First, the mathematical model, based on morphological population balance equations (MPBEs) (Ramkrishna, 2000), and capable of tracking the evolution of the whole particle ensemble in terms of the size and shape of its crystals, is presented. The model is hence used to simulate the process under a broad range of operating conditions, and of different compound-specific properties, to explore its application and potential for different systems. The results of these simulations are analyzed to identify general, system-dependent features, which constitute the basis of a compound-specific strategy for the identification of heuristically optimal operating conditions.

2.1. Mathematical modeling of the 3-stage process

2.1.1. Crystal model

The multi-faceted nature of crystals requires models capable of correctly capturing these important features. Convex polytopes (Wan et al., 2009; Borchert and Sundmacher, 2012; Singh et al., 2012) can describe the different surfaces exposed by the single crystals, but their use in MPBEs would require not only a large computational effort, but also measurement tools capable of identifying the different facets of the particles constituting the whole ensemble, and of measuring a statistically relevant sample in a short period of time. To overcome these drawbacks, and in agreement with the measurements made with the μ-DISCO (see Section 3.3), the generic particle model (Kempkes et al., 2010; Schorsch et al., 2012; Rajagopalan et al., 2017) is adopted in this work. Particles are approximated as cylinders with length L_1 and width L_2, with their shape represented by the aspect ratio $\Phi = L_1/L_2$. The particle ensemble is modeled using the particle size and shape distribution (PSSD), where the double differential $n(L_1, L_2, t)\mathrm{d}L_1\mathrm{d}L_2$ represents the number of crystals with length $L_1 \in [L_1; L_1 + \mathrm{d}L_1]$ and width $L_2 \in [L_2; L_2 + \mathrm{d}L_2]$ per unit mass of solvent.

2.1.2. General formulation of the MPBE

The general formulation of a morphological population balance equation for a well stirred batch vessel reads as follows:

$$\frac{\partial n}{\partial t} + \frac{\partial(\Gamma_1 n)}{\partial L_1} + \frac{\partial(\Gamma_2 n)}{\partial L_2} = B - E \tag{1}$$

$$n(L_1, L_2, t = 0) = n_0(L_1, L_2) \tag{2}$$

$$n(L_1 = 0, L_2, t) = 0 \tag{3}$$

$$n(L_1, L_2 = 0, t) = 0 \tag{4}$$

Here, Γ_1 and Γ_2 represent the growth or dissolution rates along the internal coordinates L_1 and L_2, the term B represents the formation of new crystals due to nucleation, breakage, and agglomeration events, while E represents the extinction term due to breakage and agglomeration. Eq. (2) is the initial condition for Eq. (1), whereas Eqs. (3) and (4) are its boundary conditions; $n_0(L_1, L_2)$ represents the particle size and shape distribution of crystals at the beginning of the process. Eq. (1) equation can be specialized, as shown elsewhere (Salvatori and Mazzotti, 2017, 2018b,a), to describe the different stages of the 3-stage process; their detailed derivation is not reported here for the sake of brevity, but is shown in the appendix. Particular focus should however be put on the constitutive equations for growth and dissolution, which have been developed among others by Ochsenbein et al. (2014) and Eisenschmidt et al. (2015) and read as follows:

$$\Gamma_i = G_i = k_{\mathrm{G},i1} \exp\left(-\frac{k_{\mathrm{G},i2}}{T}\right)(S-1)^{k_{\mathrm{G},i3}} \quad \text{with } S > 1 \tag{5}$$

$$\Gamma_i = D_i = -k_{\mathrm{D},i1} \exp\left(-\frac{k_{\mathrm{D},i2}}{T}\right)(1-S)^{k_{\mathrm{D},i3}} \quad \text{with } S < 1 \tag{6}$$

The supersaturation S, in the case of either mild non-idealities or negligible effect of the composition on the activity coefficient of the solute, can be defined as the ratio between the concentration of solute c and its solubility c^* at the temperature T:

$$S = \frac{c}{c^*(T)} \tag{7}$$

Eq. (1) is coupled with a material balance for the solute concentration, expressed in grams of solute per kilograms of solvent, which under the assumption of constant mass of solvent is

$$\frac{\mathrm{d}c}{\mathrm{d}t} = -k_{\mathrm{V}}\rho\frac{\mathrm{d}\mu_{12}}{\mathrm{d}t} \tag{8}$$

$$c(t = 0) = c_0 \tag{9}$$

Here, k_{V} is the shape factor, equal to $\pi/4$ for cylinders, ρ is the density of the crystals, and μ_{12} is one of the moments of the particle size and shape distribution, which is directly proportional to the mass of crystals suspended per unit mass of solvent and is defined according to the general cross-moment definition

$$\mu_{\mathrm{ij}}(t) = \int_0^\infty \int_0^\infty n(L_1, L_2, t) L_1^{\mathrm{i}} L_2^{\mathrm{j}} \mathrm{d}L_1 \mathrm{d}L_2 \tag{10}$$

with i = 1 and j = 2.

2.1.3. Solution of the MPBE

The MPBE is solved by discretizing Eq. (1) along the internal coordinates using 300 and 100 points for L_1 and L_2, respectively. The MPBEs for crystallization and dissolution are solved using the finite volume method, with Van Leer flux limiters for improved stability (Gunawan et al., 2004), while the MPBE for breakage is solved by exploiting the fixed pivot technique developed by Kumar and Ramkrishna (1996), to ensure the preservation of the number of fragments formed and of their mass. Simulations have been performed on a computer with an Intel(R) Xeon(R) CPU E5-2687W v3 @ 3.10 GHz processor, 20 cores, and 32 GB of RAM.

2.2. Process performance indicators

In order to quantify the quality of the products obtained at the end of both simulations and experiments, it is convenient and necessary to define average properties (see Table 1 for their definition), which are extracted by their particle size and shape distribution using the cross-moments defined in Eq. (10). In particular, the volume-weighted average length $L_{1,\mathrm{V}}$ and width $L_{2,\mathrm{V}}$ are used to identify the attainable region of the 3-stage process for both simulations and experiments. The number-weighted variances of the distribution, $\sigma_{1,\mathrm{N}}$ and $\sigma_{2,\mathrm{N}}$, and the number-weighted average sizes, $L_{1,\mathrm{N}}$ and $L_{2,\mathrm{N}}$, can be exploited to further characterize

Table 1
Performance indicators used in this work.

Volume weighted $L_{1,\mathrm{V}}$:	μ_{22}/μ_{12}
Volume weighted $L_{2,\mathrm{V}}$:	μ_{13}/μ_{12}
Number weighted $L_{1,\mathrm{N}}$:	μ_{10}/μ_{00}
Number weighted $L_{2,\mathrm{N}}$:	μ_{01}/μ_{00}
Number weighted $\sigma_{1,\mathrm{N}}$:	$\sqrt{\mu_{20}/\mu_{00} - L_{1,\mathrm{N}}^2}$
Number weighted $\sigma_{2,\mathrm{N}}$:	$\sqrt{\mu_{02}/\mu_{00} - L_{2,\mathrm{N}}^2}$

the product quality and to estimate the kinetic parameters appearing in the constitutive equations of the model, as discussed in detail in Section 4.1.4.

2.3. Parametric analysis

The aim of this work is to develop a strategy to characterize, using a small amount of experiments, the outcome of the 3-stage process when applied to compounds with different properties and characteristic kinetics. An in silico approach is certainly convenient to define such strategy, since it allows tackling this problem with a limited effort in comparison to that required for a comprehensive experimental characterization. Therefore, we have carried out first a sensitivity analysis on the operating conditions, namely the rotor speed θ and the number of cycles n_c, adopting the conditions reported in Table 3. The choice stems from the observation made elsewhere (Salvatori and Mazzotti, 2017, 2018a) that these two operating parameters have the strongest impact on product properties. The range of operating conditions investigated in this work is the one that can be effectively applied when the experimental setup described in Section 3.2 is used. This is certainly of interest and improves the information provided by the model, as it allows to acquire a more precise estimation of the outcome of the 3-stage process. The sensitivity analysis has been subsequently completed with a parametric analysis on some of the parameters appearing in the constitutive equations of the model, by varying them in physically-sound intervals. By doing so, we aim at simulating and characterizing the outcome of the 3-stage process both under a broad range of operating conditions and when compounds exhibiting different intrinsic features are considered. In particular, the analysis focuses on the growth and dissolution rates, for both characteristic dimensions, as the energy input provided by the grinding device and the mechanical properties of typical active pharmaceutical ingredients are such that it is not possible to observe a significant variation in the average sizes of the ground crystals when considering different substances (Agimelen et al., 2018). The effect of different growth and dissolution rates has been simulated by varying the pre-exponential factors, $k_{G,11}$ and $k_{D,11}$, in the range reported in Table 2. This choice is motivated by the observation that varying all the remaining parameters appearing in the growth and dissolution rates (see Eqs. (27) and (45) in the Appendix) would lead to similar conclusions. Moreover, given the linear dependence of the growth and dissolution rates on the selected parameters, it is possible to easily relate the trends observed with the change in the corresponding kinetics. It is worth noting that the absolute value of the growth or dissolution kinetics is however of limited interest in the context of studies where crystal shape is the focus, since it is the ratio of the growth and dissolution rates of the specific facets that determines the morphology of the crystals and not their absolute values (Lovette et al., 2012). The results obtained are finally rationalized to quickly identify trends characteristic to specific groups of compounds based on common features (i.e.ratio of the dissolution rates, ratio of the growth rates, etc.) and are then used to design and guide the experimental activity required to characterize the 3-stage process when applied to new systems.

2.3.1. Effect of varying the operating conditions

The third panel on the second row of Fig. 1 shows, in the L_1L_2-plane, all the possible simulated outcomes of the 3-stage process (pink circles encased by solid pink lines), adopting the simulation conditions reported in Table 3 and when $k_{G,11} = 600\ \mu m\ s^{-1}$ and $k_{D,11} = 0.818 \times 10^6\ \mu m\ s^{-1}$. It is readily observed that all the average sizes obtained at the end of the process belong to a curved quadrilateral region, whose vertices are the four colored points; we call this region the attainable region (by the 3-stage process) for a given substance and the selected seeds characteristics. Such points correspond to the outcome of the process when the combination of the minimum and maximum level chosen for the rotor speed θ (3,000 and 26,000 rpm) and the number of cycles n_c (2 and 6) are applied. Therefore, a possible experimental screening procedure to assess the feasibility of the 3-stage process for a specific new substance consists in performing these four experiments, corresponding to a two-factors factorial design, and to use the sizes of their products to define an approximated attainable region. This has the advantage of being a model-free strategy, that does not require a comprehensive characterization of the system, which is known to be extremely time demanding.

2.3.2. Effect of varying the system kinetics

However, it is necessary to verify the applicability of this method also when compounds with different properties are used. Therefore, a parametric analysis has been performed investigating the effect of different growth and dissolution kinetics. Its results are reported in the other panels of Fig. 1. Here it is possible to observe that very distinct attainable regions can be obtained for different simulated compounds, ranging from a situation where the 3-stage process actually worsens the particle size and shape when more cycles are applied (upper left corner) to a case where it greatly improves the crystal morphology leading to a wide variety of different outputs (lower right corner). It is worth noting that in all cases the outcome of the factorial design experiments can be used to delimit and define the attainable region, thus confirming

Table 2
Model parameters adopted in the simulations.

Stage	Parameter	Dimension L_1	Dimension L_2
Crystallization	$k_{G,i1}$ [$\mu m\ s^{-1}$]	600–4800	58
	$k_{G,i2}$ [K]	2400	2400
	$k_{G,i3}$ [–]	3.7	2.5
	$k_{Ho,1}$ [# $kg^{-3}\ s^{-1}$]	1.3×10^{24}	
	$k_{Ho,2}$ [–]	163	
	$k_{He,1}$ [# $kg^{-3}\ s^{-1}$]	1.4×10^{5}	
	$k_{He,2}$ [–]	10	
	$k_{S,1}$ [–]	2.5×10^{19}	
	$k_{S,2}$ [–]	0.6	
	$k_{S,3}$ [–]	0.75	
	$k_{S,4}$ [–]	2	
Milling	$k_{M,i1}$ [s^{-1}]	16.06	16.06
	$k_{M,i2}$ [–]	1.907	1.964
	$k_{M,i3}$ [μm]	30	30
	$k_{M,i4}$ [–]	$\sqrt{3}$	$\sqrt{3}$
Dissolution	$k_{D,i1}$ [$\mu m\ s^{-1}$]	$0.205–1.636 \times 10^6$	0.272×10^6
	$k_{D,i2}$ [K]	3572	3223
	$k_{D,i3}$ [–]	1	1

Table 3
Operating conditions in the simulations.

Process		Stages	
Condition	Set point	Condition	Set point
Initial temp. $T_{0,C1}$	50 °C	*Crystallization*	
Final temp. $T_{f,Cn}$	25 °C	Temp. drop ΔT_C	$(T_{0,C1} - T_{f,Cn})/n_C$
		Cooling rate γ_C	6 °C h^{-1}
Seeds mass m_0	0.1 g kg_w^{-1}	*Milling*	
Seeds	fine powder	Residence time τ	5 s
N° cycles n_C	2–6	Rotor speed θ [rpm]	3,000–26,000
		Dissolution	
		Fraction of mass dissolved m_D	40%
		Heating rate γ_D	6 °C h^{-1}

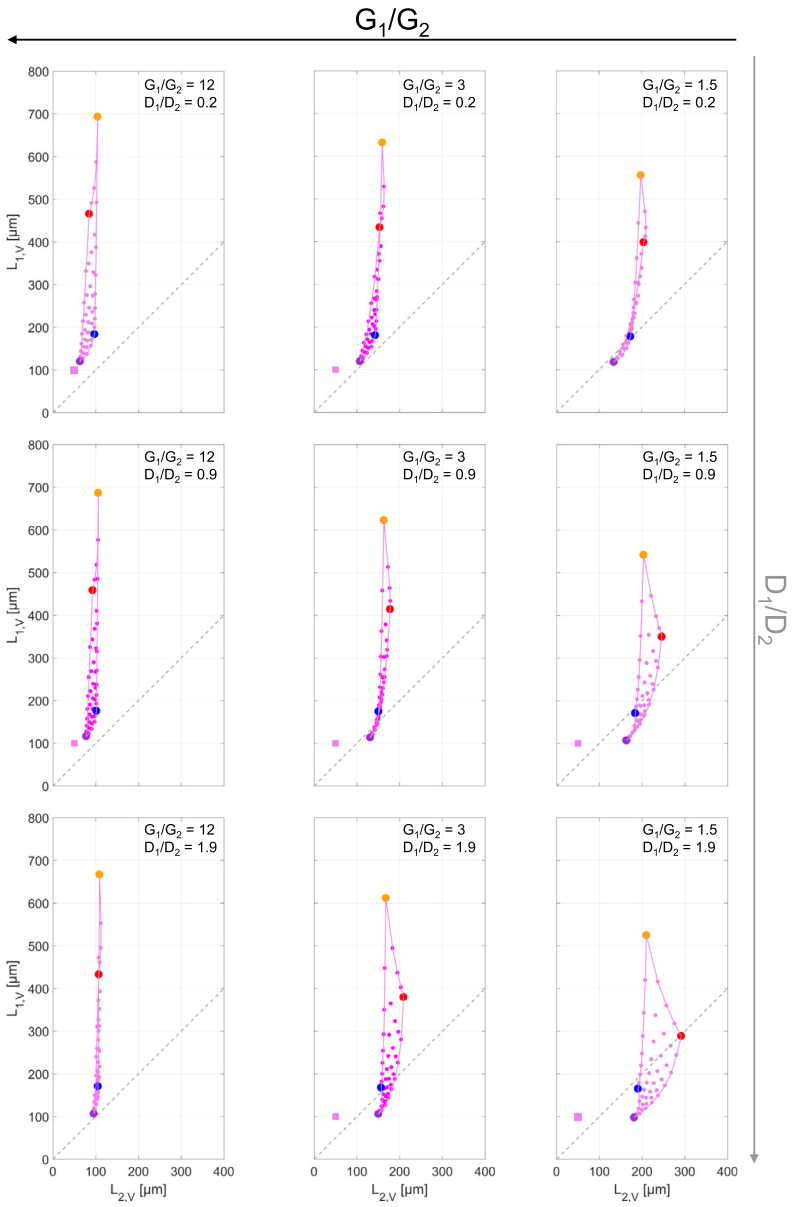

Fig. 1. Results of the sensitivity and parametric analyses performed by varying first the rotor speed θ and the number of cycles n_C (see Table 3) and subsequently the growth and dissolution kinetics to reproduce the effect of different compound properties on the achievable region of the 3-stage process. The pink dots represent all the possible outcomes obtained adopting the kinetic parameters reported in Table 2 and the conditions shown in Table 3. The solid pink line enclosing all the possible outcome of the 3-stage process represents the so called attainable region. The four experiments, indicated by the orange, red, blue, and purple markers, correspond to the four tests constituting the smart approach for process characterization. Moving from the first to the last row, as indicated by the gray arrow, the ratio of the dissolution rates for dimensions L_1 and L_2 increases. Analogously, moving across the columns from the right to the left, the ratio of the growth kinetics along both dimensions increases, as indicated by the black arrow. The values for both these properties are reported in the top-right corner of each panel. (For interpretation of the references to color in this figure legend, the reader is referred to the web version of this article.)

the suitability and robustness of the characterization strategy proposed.

In order to get a deeper understanding of the connection between compound kinetics and process outcome, it is convenient to observe how the relative position of the average sizes of the four identified experiments and their absolute position in the L_1L_2-plane changes when different kinetics are applied. To this aim, panel (a) of Fig. 2 can be used to visualize these effects. The black and gray arrows show the results of the parametric analysis when either the growth or the dissolution kinetics alone are changed, while the shaded area shows the results obtained when all the possible combinations thereof are explored. The effect of different growth rate ratios is generally more significant than that of the dissolution rates. Possible reasons for this might be that the growth stages span larger temperature intervals for cooling in comparison to that adopted for dissolution through heating, and that in the overall process there are less dissolution steps than growth steps. Furthermore, the effect of different kinetic rates appears more significant when more cycles are carried out, which is to be expected since overall more crystallization and dissolution stages are performed. The effect of a change in growth and dissolution rates reduces when high milling intensities are applied, due to the milling becoming the controlling stage in manipulating the PSSD. These effects are also visible when considering the whole attainable region. The reason for the different types of attainable region obtained lies in how the mass is removed and reprecipitated on the crystals throughout the cycles, as high dissolution rates and low growth rates along L_1 help in achieving a better morphology by

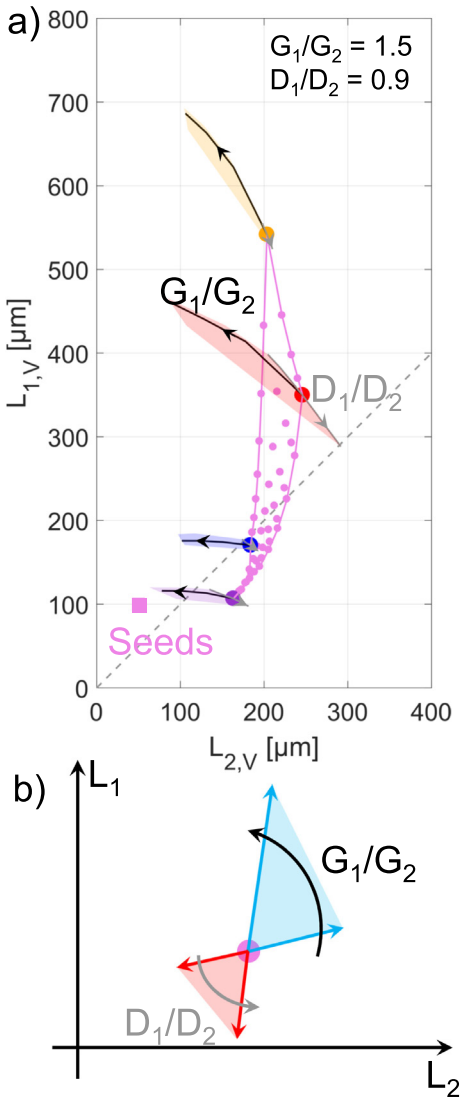

Fig. 2. In panel (a), the effect of different growth and dissolution kinetics on the four experiments used for robust and efficient process characterization is shown. The conceptualization of the phenomena leading to the different types of attainable regions are shown in panel (b). Here, for different growth and dissolution rates, the evolution of the sizes of an exemplary particle during growth and dissolution is shown.

reducing the characteristic length and by favoring the growth along the width, while the opposite situation occurs for high G_1/G_2 ratios and low D_1/D_2 ratios. A conceptualization of these effects is illustrated in Fig. 2(b), where the blue arrows and the comprised region represent an exemplary evolution of the particle sizes for different G_1/G_2 (black arrow) during cooling, while the red arrows and the region between them represent the evolution of the sizes for different D_1/D_2 (gray arrow) ratios during the dissolution stage.

2.3.3. Effect of varying the seeds characteristics

To verify how the type of attainable region obtained at the end of the 3-stage process depends on the characteristics of the seeds, we extended the parametric analysis by performing simulations where the mass of seeds and their PSSD are varied. Table 4 reports the characteristics of the seeds used at the beginning of each simulation, while Fig. 3 shows the attainable regions for the three cases considered. As it is readily observed, the shape of the region obtained for the three cases is the same, with the characteristics of the seeds having only an effect on the final average sizes. This observation is of great relevance, as it demonstrates that the type of attainable region does indeed only depend on the intrinsic properties of the compound to which the 3-stage process is applied and not on the PSSD or on the amount of the seeds used.

Table 4
Seeds used in simulations.

Simulation	Seeds	Seeds properties	Seeds mass m_0
Sim1	Seeds 1	Gaussian $\mu_{L_1} = 100$ μm and $\mu_{L_2} = 50$ μm	0.1 g kg_w^{-1}
Sim2	Seeds 1		0.025 g kg_w^{-1}
Sim3	Seeds 2	Gaussian $\mu_{L_1} = 500$ μm and $\mu_{L_2} = 50$ μm	0.1 g kg_w^{-1}

2.3.4. Factorial design

The results of the parametric analysis are very important, as they have allowed us to identify a smart, robust, and effective experimental screening procedure required to investigate the feasibility and potential of the 3-stage process with neither a thorough characterization of compound specific properties nor system-specific mathematical modeling. This procedure consists in performing four experiments, under operating conditions defined by combining the minimum and maximum applicable milling intensity and number of cycles, and defining the attainable region as the portion of the L_1L_2-plane enclosed by the average sizes of the corresponding products. Furthermore, the simulations showed that the type of attainable region obtained depends only on the ratio of growth rates G_1/G_2 and dissolution rates D_1/D_2 typical of the compound used.

A few remarks are necessary. The first concerns the quality of the characterization of the process outcome obtained with the factorial design approach. As shown in previous publications (Salvatori and Mazzotti, 2017, 2018a), the dependence of the final size and shape of the crystals on the operating conditions is strongly non-linear. Nevertheless, the approximated achievable region, obtained with the approach proposed in this work, still represents a good indication of the process outcome and can be used as a guide throughout the process design stage, where decisions concerning the operating conditions are made.

The second remark concerns the improvement in product properties achieved when the compound exhibits high G_1/G_2 and low D_1/D_2 ratios. The reduced variability in process outcome obtained shows that the final size and morphology of the crystals cannot be significantly improved by increasing the number of cycles performed. Nevertheless, the 3-stage process, due to the repeated milling and dissolution stages, allows to obtain crystals that are more compact than those obtained by simple cooling, as well as a final powder with a reduced presence of fines in comparison to that obtained by simple milling.

The strategy for process characterization developed in this chapter will be assessed with a dedicated experimental campaign using two different compounds, namely β L-Glutamic acid and γ D-Mannitol. For the latter, however, it is necessary to estimate the specific growth rates in order to relate its properties to the type of attainable region obtained. To this aim, the fourteen cooling stages performed belonging to the four factorial experiments can be used. This is of particular interest, given that a deeper insight and characterization of the system can be obtained without performing any other experiments. Therefore, a preliminary in silico study has been carried out to assess the possibility of using the information of the fourteen cooling stages to estimate growth kinetics.

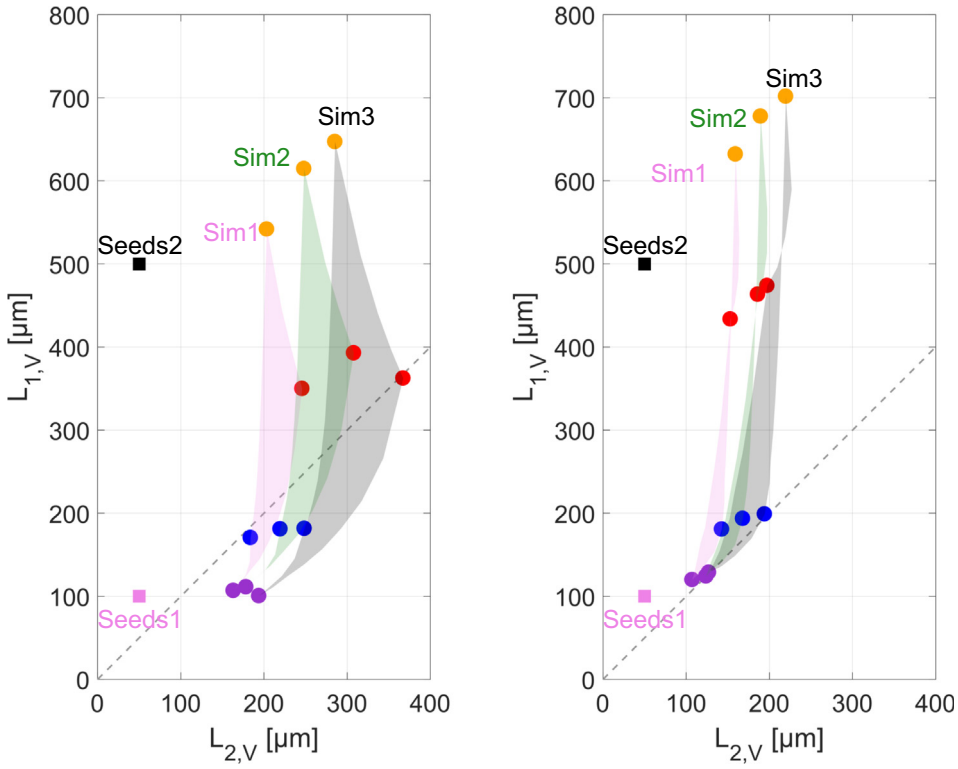

Fig. 3. Results of the analysis performed to investigate the effect of different seed populations and mass thereof, as reported in Table 4, on the attainable region of the 3-stage process for two sets of kinetic parameters (when $G_1/G_2 = 1.5$; $D_1/D_2 = 1.9$ and $G_1/G_2 = 3$; $D_1/D_2 = 0.2$, respectively).

2.4. Fitting of the kinetic parameters

In this paper, we estimate the growth kinetics of γ D-Mannitol exploiting the information available from the four experiments performed according to the factorial design approach. The estimation is performed by minimizing the objective function defined as

$$F(\mathbf{p}) = \frac{N_E}{2}\sum_{i=1}^{N_O}\ln\sum_{j=1}^{N_E} w_{ij}\left(\frac{y_{ij}-\hat{y}_{ij}(\mathbf{p})}{y_{ij}}\right)^2 \tag{11}$$

where $\mathbf{p}$ represents the set of growth kinetic parameters to be estimated, N_E is the number of experimental measurements, N_O is the number of fitted outputs (average properties of the measured PSSD), y_i represents any average property of the measured particle size and shape distribution for the i-th experiment that needs to be fitted, $\hat{y}_i(\mathbf{p})$ is the corresponding model estimate based on the set of parameters $\mathbf{p}$, and w_{ij} is used to weight the contribution of each relative error to the objective function. To identify the minimum of the function $F(\mathbf{p})$, the genetic algorithm provided by the Matlab optimization toolbox is used. The algorithm is seeded using 50% of the individuals randomly generated using latin hypercube sampling and 50% from the last population of the previous run. The population size chosen is 60, with a crossover fraction of 0.70.

While on the one hand fitting the whole particle size and shape distribution would be of great interest, on the other hand this would lead to a very high computational burden. Therefore, in this work we aim at fitting the number-weighted average sizes and variances reported in Table 1, which allow identifying uniquely the whole distribution of crystals with a reduced simulation effort.

2.4.1. Confidence intervals estimation

Along with the kinetic parameters, we also estimate the corresponding confidence intervals by means of the Jacobian analysis.

The diagonal element S_{ii} of the error covariance matrix can be calculated as

$$S_{ii} \approx \sigma^2_{E,i} = \frac{1}{N_E}\sum_{j=1}^{N_E}\left(y_j - \hat{y}_j(\mathbf{p}^*)\right)^2 \tag{12}$$

By linearizing the model and assuming normally distributed errors, the positive semidefinite covariance matrix $\mathbf{V}$ can be estimated using the corresponding Jacobian matrix as

$$\mathbf{V} \approx \left(\mathbf{J}^T\mathbf{S}\mathbf{J}\right)^{-1} \tag{13}$$

This matrix can be used to determine the hyperellipsoid defined at the confidence level α corresponding to the approximate confidence intervals for the estimated parameter j.

$$C_j = \sqrt{V_{jj}}\, t^{N-k}_{1-\alpha/2} \tag{14}$$

In Eq. (14), $t^{N-k}_{1-\alpha/2}$ corresponds to the value of the t-statistics with $N-k$ degrees of freedom at the designed confidence level α. The estimated confidence intervals are certainly affected by the uncertainty introduced with the linearization hypothesis, but they provide nevertheless the information required to evaluate the quality of the fitting.

2.5. Estimation of growth kinetics from in silico data

In order to assess the possibility of estimating the growth rate parameters using the information associated to the fourteen cooling stages performed at different operating conditions while carrying out the complete factorial design protocol, the in silico data generated by the model in the course of the corresponding simulations can be used. In particular, the time-resolved number-weighted average $L_{1,N}$ and $L_{2,N}$ are fitted to estimate the value of the kinetic parameters appearing in Eq. (27) for both crystal dimensions. In order to reproduce the effect of the experimental error and measurement uncertainties on the measured sizes, white Gaussian noise is added to the simulated data, using the in-built

Matlab function *awgn*, thus generating in silico a set of experimental data.

Panel (a) of Fig. 4 shows the in silico generated experimental data (red boxes), while the results of the fitting are reported as a blue solid line. For the sake of clarity and brevity, only the results of 3 out of the 14 available cooling stages are shown. The quality of the fitting is satisfactory, with a good quantitative agreement (average absolute error of 10 μm for both dimensions) between the two sets of data. Panel (b) shows, in the concentration vs.temperature plane, the region explored by the different simulated stages (red area) and the solubility curve (black line): the range of validity of the fitting covers a broad range of temperatures and concentrations. It is worth noting that the region partially lies below the solubility line, which corresponds to the conditions of the solution at the beginning of the cooling stages; this is due to the final conditions of the simulated dissolution stage, as the simulations are stopped at a close-to-equilibrium concentration. Finally, even if for some of the cooling stages the initial and final temperatures are the same, the different particle ensembles suspended, both in terms of number of crystals and sizes of the particles, lead to a different evolution of the concentration throughout the stages, thus making these stages actually different and allowing to effectively exploit all the cooling steps for the estimation of the kinetics.

3. Experimental

3.1. Materials

The compounds used in this work are D-Mannitol (Sigma-Aldrich, ⩾ 98%, Switzerland) and L-Glutamic acid, produced by pH-shift from L-Glutamic acid monosodium monohydrate (Sigma-Aldrich, ⩾ *slant*98%, Switzerland) and hydrochloric acid (Fluka, Buchs, Switzerland, 37–38%) according to the precipitation procedure reported elsewhere (Cornel et al., 2009; Schöll et al., 2006).

As highlighted by Cornel et al. (2010), D-Mannitol has three different polymorphs, whose solubilities in water are reported in panel (a) of Fig. 5. In this work we focus on the thermodynamically stable polymorph γ, exhibiting a needle-like morphology. However, to reduce the very large solubility of D-Mannitol in the solvent and to avoid the formation of bacteria colonies in suspension, the solvent used in the experimental campaign is a mixture of water (Millipore Milli-Q, Zug, Switzerland) and propan-2-ol (Reagent grade, VWR, Germany), which is an antisolvent for D-Mannitol. Therefore, the solubility of γ D-Mannitol is measured according to the experimental procedure described in Section 3.4. The seeds used for the factorial experiments described in Section 3.5 consist of the fine powder delivered as a raw chemical without further

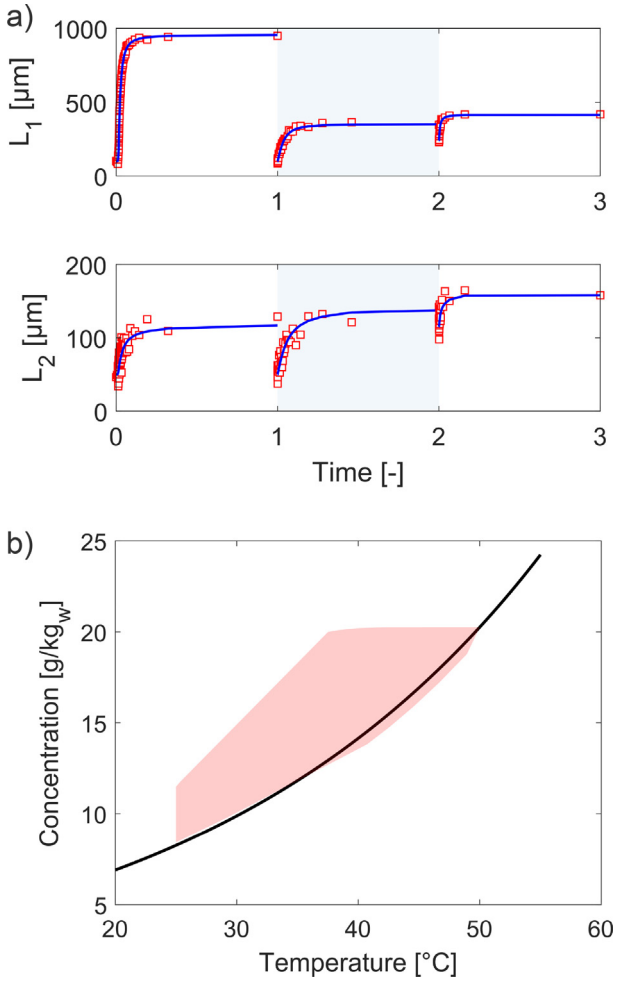

Fig. 4. Results of the in silico fitting performed to assess the possibility of estimating growth kinetics using the data available when the factorial experiments are performed. In (a) the fitted average sizes are shown, while panel (b) shows the range of concentration and temperatures over which the fitting is performed.

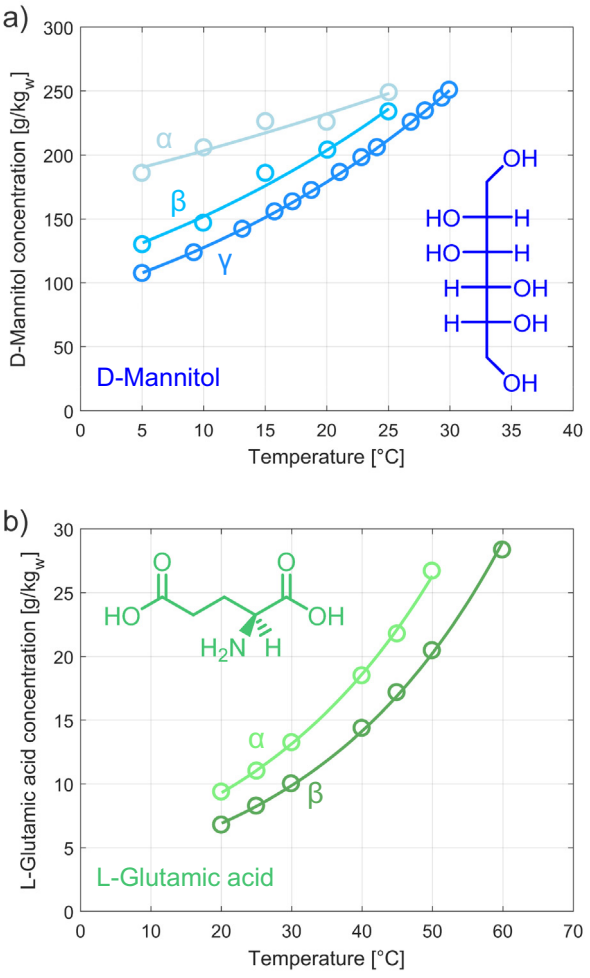

Fig. 5. Solubility of the model compounds and their polymorphs. Panel (a) shows the solubility in water of the three polymorphs of D-Mannitol, the metastable α and β, and the stable γ, as reported by Cornel et al. (2010). In panel (b) the solubility of α and β L-Glutamic acid from Schöll et al. (2006) are plotted.

treatment. The corresponding particle size and shape distribution is reported on the right-hand side of Fig. 6.

L-Glutamic acid has two polymorphic forms, namely the metastable α form and the thermodynamically stable β form, which are monotropically related (Schöll et al., 2006). The corresponding solubilities are reported in panel (b) of Fig. 5. The seeds of β L-Glutamic acid used throughout the experimental campaign were obtained by polymorphic transformation from the α form via pH-shift, and their particle size and shape distribution is shown in the left-hand side of Fig. 6.

3.2. Experimental setup

In Fig. 7, a sketch of the laboratory setup is shown. The experimental rig consists of two crystallizers, a continuous rotor-stator wet mill (IKA MagicLab, Module MK), and a peristaltic pump (Ismatec BVP). In order to keep the temperature of the suspension constant during milling, the grinding chamber is jacketed and connected to a thermostat. Moreover, each crystallizer is equipped with a dedicated thermostat for the precise control of the suspension temperature during crystallization and dissolution and with a dedicated ATR-FTIR spectrometer (ReactIR 45m, Mettler Toledo, Switzerland), used to monitor the concentration of D-Mannitol in the liquid phase. An FBRM G400 (Mettler Toledo, Switzerland) is used to monitor possible nucleation and attrition events. This device is used only to detect the formation of fine particles, since the extraction of quantitative information on the size and shape of non-equant particles from FBRM measurements is known to be troublesome.

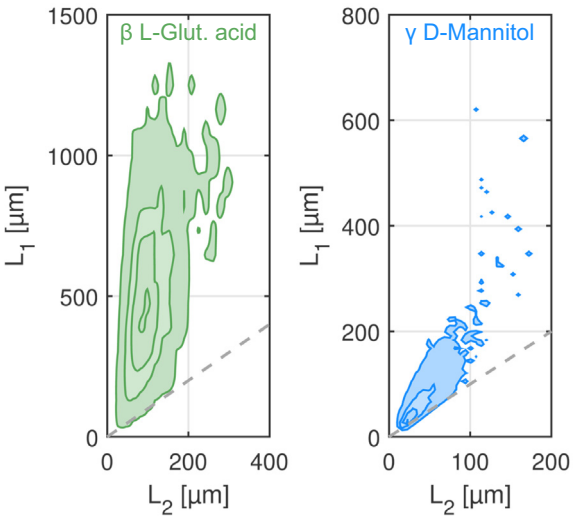

Fig. 6. Volume-weighted average particle size and shape distributions of the seeds of γ D-Mannitol (left) and β L-Glutamic acid (right) used for the factorial experiments.

3.3. PSSD measurement setup and protocol

The PSSD of the products is measured by using the µ-DISCO, a stereoscopic imaging device, described by Rajagopalan et al. (2017). It consists of two cameras, equipped with telecentric lenses, arranged in an orthogonal configuration, thus allowing for the reconstruction of the particle shape starting from two orthogonally projected images of the same crystal. Pictures of the particle suspension, flowing in a quartz cell engineered to ensure lowest optical distortion, are collected through bursts with a frame rate of 35 fps. For each measurement, 10 bursts of 800 images each are launched, thus allowing to reconstruct the size and shape of approximately 30,000 particles in a time interval of 15 min. Based on the reconstructed geometrical properties, the particles are automatically classified in 5 classes, namely spheres, cuboids, needles, platelets, and non-convex polytopes. In this work, we only consider the needles and cuboids classes, as we believe, based on visual inspection under the optical microscope, that other crystal shapes occasionally detected are not representative of the crystal population. Because of the high suspension density, reaching 7 wt% in the case of γ D-Mannitol, the measurements are performed off-line on a suspension in antisolvent.

3.4. Solubility of γ D-Mannitol

In this work, the solubility of γ D-Mannitol in a 10/90 wt% mixture of propan-2-ol and water is measured in the temperature

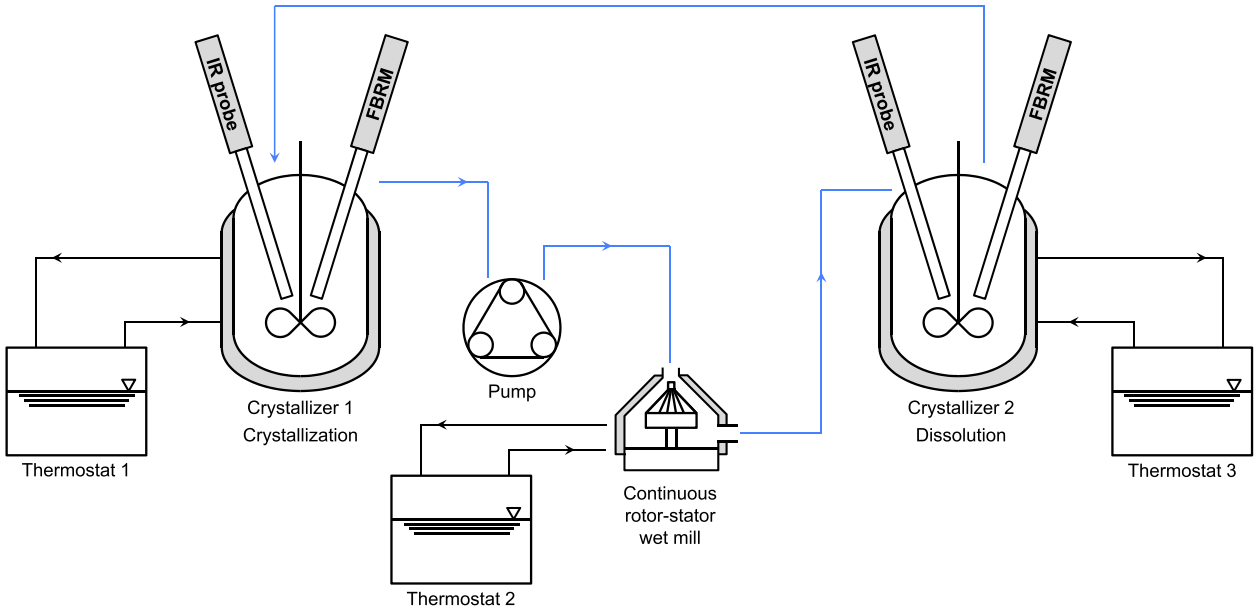

Fig. 7. Scheme of the laboratory setup. Note that the pump can be used to move the suspension from Crystallizer 1 to Crystallizer 2 and viceversa.

range 3–30 °C using both a gravimetric method and an ATR-FTIR-based approach.

To perform the gravimetric analysis, a suspension is prepared by adding to 500 g of the propan-2-ol/water mixture, kept at the target temperature T, an excess of solids. The suspension is then kept at T under stirred conditions for 24 h. Three samples of the liquid phase are then taken and dried on Petri dishes in a ventilated oven at 25 °C for 24 h. The weights of the empty, full, and dried Petri dishes are recorded, thus allowing to evaluate the solubility.

The solubility is also assessed with chemometrics measurements. To correctly capture both the effect of temperature and concentration on the infrared signal, a first set of calibration experiments has to be performed to fit the concentration to the characteristic peaks. Here, 2 kg of the propan-2-ol/water mixture are prepared at temperature T_0 in a stirred jacketed crystallizer, equipped with an FBRM probe to detect possible nucleation events. γ D-Mannitol is added to produce an undersaturated solution (saturated at T_S), which is then cooled down to the final temperature T_F at a rate of 5 °C h^{-1}. The IR spectra are collected until either the final temperature is reached or nucleation is detected. The results of the calibration experiments are used to train a model based on partial least squares regression (PLS), which correlates the intensity of the baseline-corrected spectra to the concentration of the solution characteristic of each experiment at different temperatures. To this aim we used the Matlab function *plsregress* with 10-fold cross validation and four latent variables. Fig. 8 shows the set of experiments performed under the conditions reported in Table 5 and according to the procedure described above. The experiments have been repeated twice and allow calibrating robustly the ATR-FTIR over a broad range of concentrations and temperatures. In the upper part of panel (b), the raw spectra collected during the experiments are reported along with that of the solvent mixture (blank experiment). In order to correlate the peak intensity with the concentration of γ D-Mannitol in solution, a single-point baseline correction is applied, using as a reference the intensity at 1127 cm^{-1} wavenumber. The choice is motivated by the fact that the spectrum of propan-2-ol exhibits a maximum at that wavenumber, and its concentration in the solvent mixture remains constant. Hence, its absorbance at a given temperature should be equal at any given solute concentration. This assumption is confirmed by visual inspection of the spectra collected at various conditions, and the choice of the baseline results in consistent spectra among the repetitions of the same experiments. The PLS regression is performed in the wavenumber range 1127 to 999 cm^{-1}, where the characteristic peaks of γ D-Mannitol show the maximum variability upon changes in concentration and are least affected by those of the solvent. The results of the baseline correction are reported in the lower plot of panel (b).

Table 5
List of the ATR-FTIR calibration and solubility measurements.

Exp ID	m_W [g]	m_P [g]	m_M [g]	T_0 [°C]	T_F [°C]	T_S [°C]
Blank	1799.9	200.1	0	30	3	–
Exp1	1800.6	200.9	365.18	40	20	30
Exp2	1799.9	200.7	258.60	30	10	20
Exp3	1800.4	200.9	154.64	15	3	5
Exp4	1799.7	200.2	144.59	15	3	3
Val1	1800.5	200.5	233.30	5	15	n/a
Val2	1799.9	200.0	329.30	15	25	n/a
Val3	1800.2	200.3	391.42	20	30	n/a
Val4	1800.3	201.5	395.04	25	30	n/a

The solubility is estimated by performing four dedicated experiments, where 2 kg of the propan-2-ol/water mixture are prepared at four different initial temperatures. An excess of γ D-Mannitol is

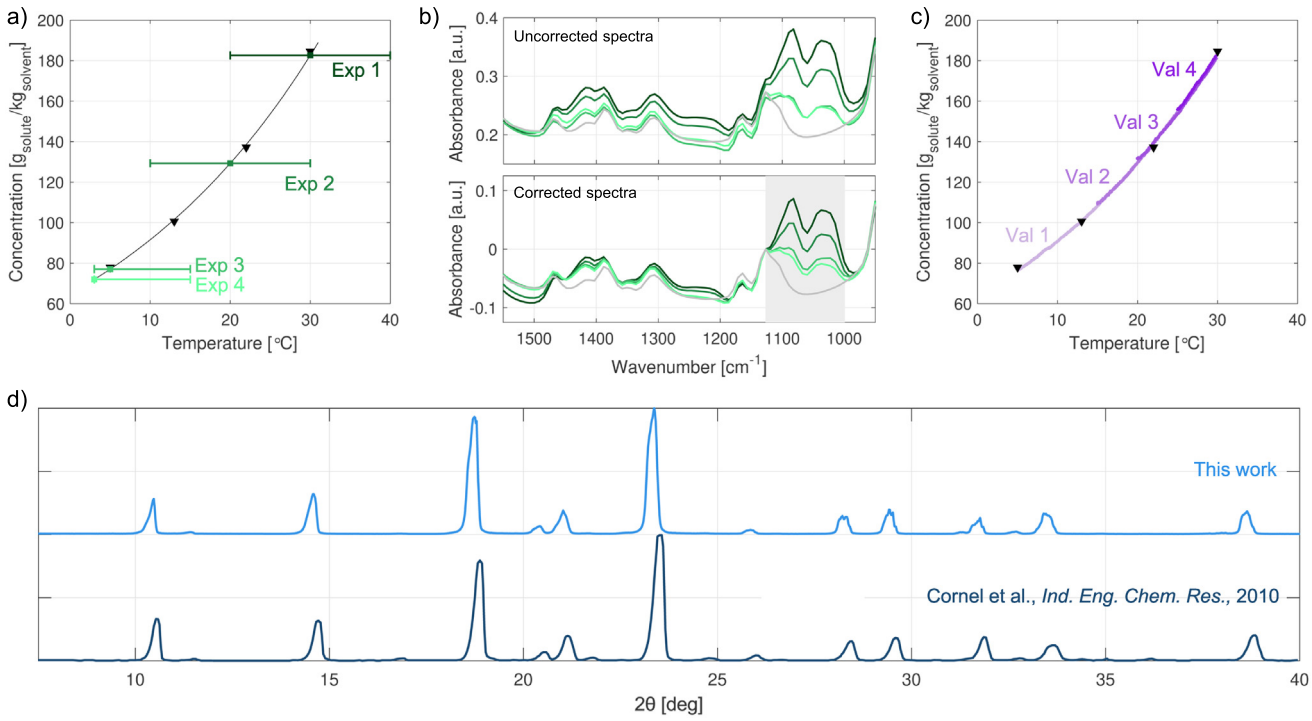

Fig. 8. (a) Range of concentrations and temperatures explored with the calibration experiments. The black triangles correspond to the gravimetric data of solubility which were fitted with an exponential function (black line). (b) In the upper plot, the raw spectra collected for each calibration experiment at saturated conditions according to the gravimetric measurements are reported. The spectrum of the blank experiment in gray was collected at 20 °C. In the lower plot, the same spectra, after applying the baseline correction, are shown and the range of wavenumbers used by the PLS algorithm is highlighted. (c) Concentration profiles of the solubility experiments as estimated from ATR-FTIR measurements compared with the gravimetric data. (d) Comparison between the XRPD pattern obtained by Cornel et al. (2010) for γ D-Mannitol and that obtained in this work.

added and the system is kept under constant conditions for two hours. The suspension is then heated at a rate of 2 °C h^{-1} until the final temperature is reached. The results of the solubility measurements, carried out under the conditions in Table 5, are shown in panel (c) with purple markers. Here, a comparison with the data acquired with gravimetric measurements (represented by the black triangles) is carried out. The good agreement between the results obtained with different techniques assesses the possibility of measuring accurately the solute concentration throughout the experimental campaign.

To check the possible influence of the different solvent on the solid form, an X-ray powder diffraction measurement (XRPD) is performed on the crystals recovered at the end of the experiments. Panel (d) of Fig. 8 shows the results of the XRPD measurement as obtained by Cornel et al. (2010) in water and those obtained in this work for γ D-Mannitol in the water/propan-2-ol mixture. Being the two patterns identical, we conclude that the change of solvent did not impact the solid form produced at the end of the crystallization process.

3.5. 3-stage process experimental protocol and factorial design

A saturated solution of the specific compound in the corresponding solvent is prepared at the initial temperature $T_{0,C1}$. The required amount of seeds m_0 is added and the system is cooled to the final temperature of the first cooling stage $T_{f,C1}$ at the rate γ_C. The system is kept at constant temperature until equilibrium is approached. The suspension of crystals is pumped at 0.98 L min^{-1} through the continuous rotor-stator wet mill, operated at the desired rotor speed θ. The outcome is collected in a second crystallizer, where it is heated to the temperature $T_{f,H1}$, chosen to ensure that, in the proximity of equilibrium, the fraction of suspended mass m_D will be dissolved. The dissolution step is necessary to eliminate most of the fine particles formed during the milling stage, and the value of m_D has to be carefully chosen so as to accomplish the task without reducing the efficiency of the overall process. The stages are repeated n_C number of times until the final temperature $T_{f,Cn}$ is reached. Then the crystals are collected, filtered, and washed with pure propan-2-ol to promote displacement of the entrained solution, thus avoiding its crystallization during drying. Finally, the washed filter cake is placed in a ventilated oven at 65 °C for 24 h.

4. Results and discussion

4.1. Factorial design for the 3-stage process

In this section we aim at assessing the strategy described above by applying it experimentally to two different compounds, namely β L-Glutamic acid and γ D-Mannitol, both crystallized from specific aqueous solutions. In particular, for each of them, the four factorial experiments are carried out to identify the corresponding attainable region. To relate the type of attainable region obtained for the two compounds to their specific properties, an estimation of the growth kinetics for γ D-Mannitol is performed and the estimated kinetics are compared to those already available for β L-Glutamic acid. Based on these results and on the process simulations, a general system-dependent strategy to identify heuristic optimal conditions is proposed.

4.1.1. Case study 1: β L-Glutamic acid

Given that the effectiveness of the 3-stage process in modifying the size and shape of β L-Glutamic acid crystals has already been evaluated both experimentally and in silico and thoroughly discussed elsewhere (Salvatori and Mazzotti, 2017, 2018a), we report here results for this compound as a reference case, aiming at highlighting how the well-known properties of this system can be used to interpret the outcome of the process based on the general trends observed through the simulations presented above.

The 3-stage process is applied according to the operating conditions in Tables 6 and 7, and the resulting volume-weighted average characteristic dimensions of the final crystal population are shown for each of the factorial experiments together with the full PSSDs in the left-hand side of Fig. 9. One can readily observe that the number of cycles significantly affects the width L_2 of the crystals, thus leading to a wide attainable region. This is a case where the process we consider is most effective in navigating the space plane by changing the relative dimensions of the crystals, and both the milling intensity and the number of cycles have an evident impact on the final crystal shape.

With reference to the simulations illustrated in Fig. 1, the behavior of β L-Glutamic acid is similar to that corresponding to the three cases at bottom right corner of the figure, i.e. for small values of the ratio G_1/G_2 when the ratio D_1/D_2 is large or intermediate, and for large values of the ratio D_1/D_2 when the ratio G_1/G_2 is small or intermediate.

4.1.2. Case study 2: γ D-Mannitol

The results of the six experiments performed according to the operating conditions reported in Tables 6 and 7 are shown in the

Table 7
Rotor speed and number of cycles of each experiment of the factorial design for the model compounds.

β L-Glutamic acid			γ D-Mannitol		
	θ [rpm]	n_C		θ [rpm]	n_C
A1	3,000	2	M1	5,000	2
A2	3,000	6	M2	5,000	5
A3	14,000	2	M3	15,000	2
A4	14,000	6	M4	15,000	5
			M5	25,000	2
			M6	25,000	5

Table 6
Operating conditions of the factorial design for β L-Glutamic acid (LGA) and γ D-Mannitol (DM).

Process			Stages		
Condition	LGA	DM	Condition	LGA	DM
Initial temp. $T_{0,C1}$ [°C]	50	25	*Crystallization*		
Final temp. $T_{f,Cn}$ [°C]	25	5	Temp. drop ΔT_C	$(T_{0,C1} - T_{f,Cn})/n_C$	
			Cooling rate γ_C [°C h^{-1}]	6	2
Seeds mass m_0 $\left[\text{g kg}_{\text{solv}}^{-1}\right]$	0.1	7.8	*Milling*		
N° cycles n_C	varying		Residence time τ [s]	5	
			Rotor speed θ [rpm]	varying	
			Dissolution		
			Fraction of mass dissolved m_D	40%	20%
			Heating rate γ_D [°C h^{-1}]	6	2

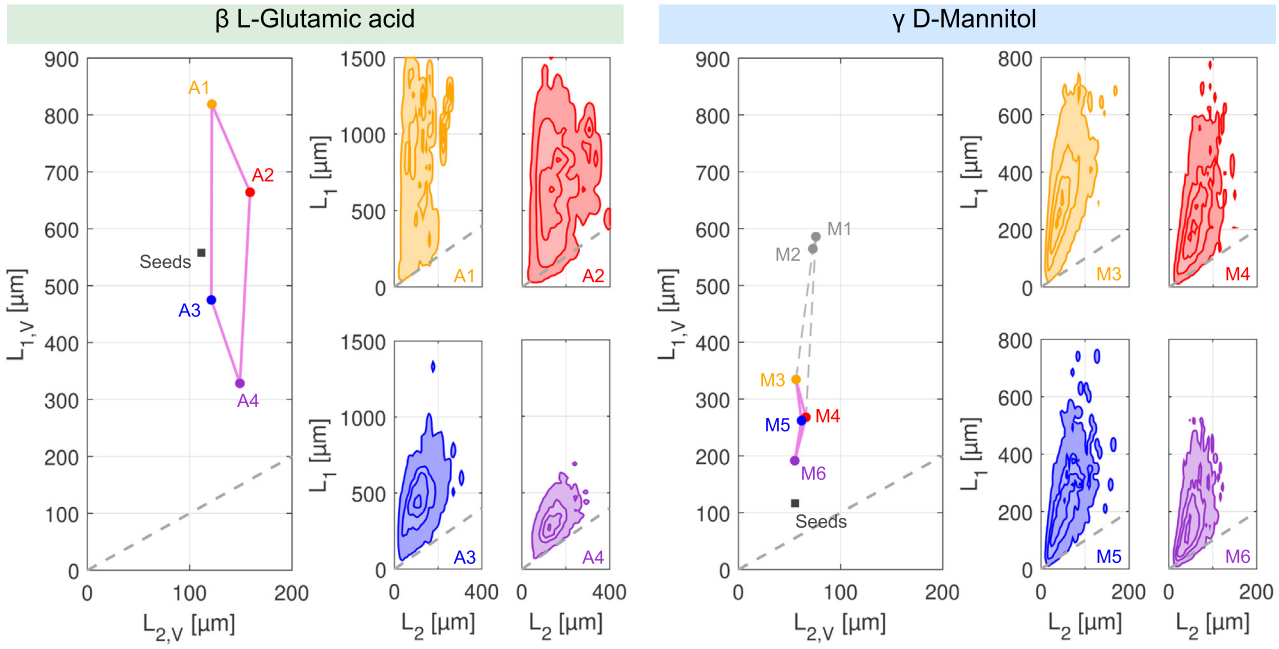

Fig. 9. Results of the factorial design applied to β L-Glutamic acid and γ D-Mannitol. For each case, on the left, the volume-weighted average sizes of the products as measured by the μ-DISCO are shown and the enclosed attainable region is defined by the fuchsia line. The PSSDs for the products of every factorial experiment are reported on the right-hand side of the corresponding plots.

right-hand side of Fig. 9; for each experiment the volume-weighted average length and width of the final population of crystals are plotted along the full PSSDs.

Inspection under the optical microscope of the crystals obtained in experiments M1 and M2, performed at 5,000 rpm, showed the presence of crystals exceeding the millimeter in length together with a considerable amount of fines. This condition is not optimal for sizing with the μ-DISCO, because due to optical constraints the number of larger crystals would likely be underestimated, with a strong bias in the volume-based average $L_{1,V}$ towards fines. For this reason, we have chosen to include these experiments for the characterization of the attainable region, but we have decided not to exploit their information for the estimation of the growth kinetics.

One can observe that in all the experiments considered the process does not lead to a significant variation in the width of the crystals L_2. With reference to the simulations illustrated in Fig. 1, the behavior of γ D-Mannitol is similar to that corresponding to the five systems along the diagonal of the G_1/G_2-D_1/D_2 plane in the figure; this corresponds to where the ratios G_1/G_2 and D_1/D_2 are simultaneously small, intermediate, or large.

4.1.3. Discussion

In the case of β L-Glutamic acid the growth and dissolution rates of the different facets is known from the literature; thus the ratio G_1/G_2 can be calculated to be about 4 (Ochsenbein et al., 2014), whereas the ratio D_1/D_2 is about 12 (S. Bötschi and A. K. Rajagopalan, personal communication, 2018). This puts β L-Glutamic acid in the bottom right corner of Fig. 1, corresponding to systems for which the 3-stage process allows tuning the PSSD by varying the operating conditions. The experimental results presented in Section 4.1.1 and illustrated in the left-hand side of Fig. 9 are perfectly consistent with the prediction from the values of the ratios G_1/G_2 and D_1/D_2.

Such ratios are in contrast not known for γ D-Mannitol, for which we have however the outcome of the experiments carried out according to the factorial design (see Section 4.1.2 and the right-hand side of Fig. 9). Such experiments point at a system where both ratios G_1/G_2 and D_1/D_2 are small, or intermediate, or large (in relative terms). In order to confirm this systems property, we should either carry out a full-fledged characterization of growth and dissolution kinetics, i.e. a task beyond the scope of this work, or alternatively use the available cooling steps performed during the factorial design experiments in order to obtain a best estimate of the growth kinetics (as discussed in Sections 2.4 and 2.5). The latter approach will be pursued in the following.

4.1.4. Empirical estimation of γ D-Mannitol growth kinetics

From the experiments reported in Section 4.1.2, there are nine cooling stages that can be used for the empirical characterization of the γ D-Mannitol growth rates. For each cooling stage we have measured the solute concentration continuously and the PSSD of the starting and of the final ensemble of crystals. These data are shown in the two panels of Fig. 10, where the data of the nine cooling stages are concatenated and plotted as function of a rescaled time (horizontal axis), with the actual duration of each step reported in the upper panel. Both panels show the measured solute concentration in grams of solute per kilogram of solvent (light blue profiles, left vertical axis). The final number-weighted average length of the crystals, $L_{1,N}$, and variance along the L_1 direction, $\sigma_{1,N}$, are also shown in the upper and in the lower panel, respectively (pink circles, referring to the right vertical axis). Fig. 11 illustrates particle size and shape properties for two exemplary experiments, namely Exp 1 and Exp 2 in Section 4.1.2: in the upper part of Fig. 11 the PSSDs of the crystal ensemble as measured using μ-DISCO before cooling (pink contour lines and shade) and thereafter (gray) are illustrated; in the lower part of the same figure the two final PSSDs are illustrated as blue contour lines.

By inspection of Fig. 11, it is apparent that the final crystals are more elongated, with a broader distribution in the L_1 direction than the initial crystals. This is confirmed by the initial and final values of $L_{1,N}$ and of $\sigma_{1,N}$ in Fig. 10: both quantities increase significantly during cooling because of growth, obviously, and because of broadening of the distribution. The latter effect is much less obvious, and might require a more in-depth study for a sound physically based characterization. In the scope of this work, we have

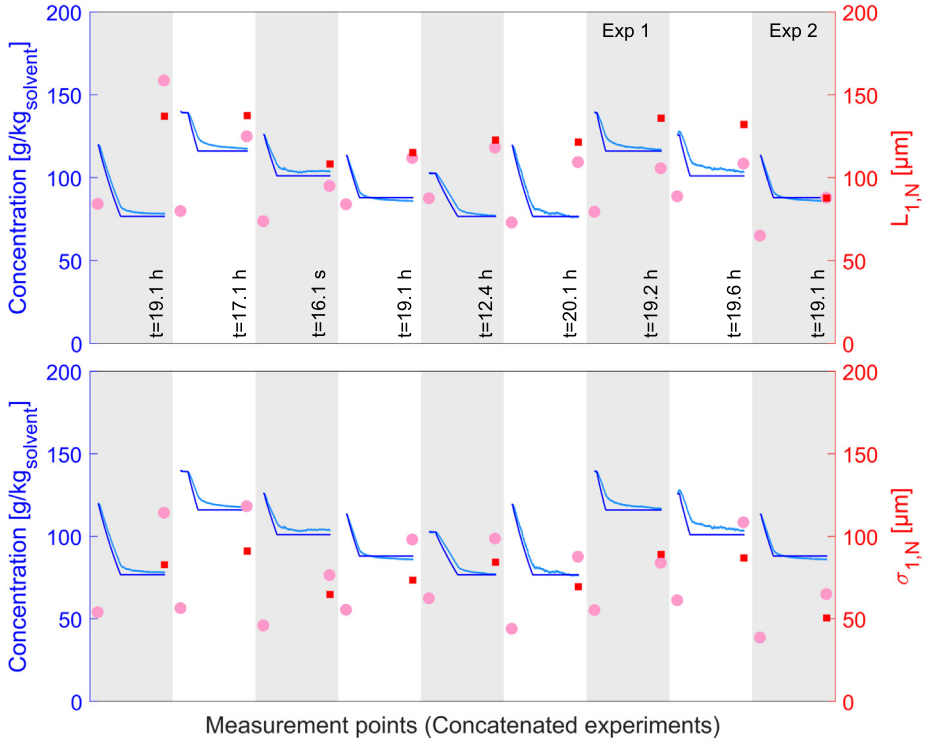

Fig. 10. Results of the fitting aimed at estimating the growth kinetics for γ D-Mannitol starting from the cooling stages carried out during the factorial experiments. The light blue markers correspond to the measured concentration profile, while the pink circles correspond to the number-weighted average $L_{1,N}$ (upper panel) and $\sigma_{1,N}$ (lower panel) at the beginning and end of each stage. The dark blue line and the red squares represent the fitted concentration and $L_{1,N}$ and $\sigma_{1,N}$ respectively. For each stage, the corresponding duration of the experiment is reported. (For interpretation of the references to color in this figure legend, the reader is referred to the web version of this article.)

decided to describe such effect via a growth model, where the growth rate in the L_1 dimension is size-dependent: the functional form is known to be able to account for a broadening of the distribution (see for instance the characterization of β L-Glutamic growth reported earlier (Ochsenbein et al., 2014)).

In this work we propose the following constitutive equations for the growth rate in the two directions as a function of supersaturation, temperature and dimension L_1 (depending on seven parameters):

$$G_1 = p_{11} \exp\left(-\frac{p_{12}}{T}\right)(S-1)^{p_{13}}\left(1-\exp\left(-p_{14}\frac{L_1}{L_{\text{ref}}}\right)\right) \tag{15}$$

$$G_2 = p_{21} \exp\left(-\frac{p_{22}}{T}\right)(S-1)^{p_{23}} \tag{16}$$

It turns out that the nine experiments available are not sufficient to estimate all seven parameters without a strong correlation among them. We have therefore simplified the previous equations by neglecting the explicit dependence on temperature, i.e. by setting $p_{12} = p_{22} = 0$ (note that the equations are still temperature-dependent through the definition of supersaturation in Eq. (7)), by assuming linear dependence on the supersaturation driving force, i.e. by setting $p_{13} = p_{23} = 1$, and by choosing $L_{\text{ref}} = 1000$ µm. The resulting simplified equations depending only on three parameters, namely p_{11}, p_{14}, and p_{21}, are:

$$G_1 = p_{11}(S-1)\left(1-\exp\left(-p_{14}\frac{L_1}{L_{\text{ref}}}\right)\right) \tag{17}$$

$$G_2 = p_{21}(S-1) \tag{18}$$

The three parameters have been estimated by matching simulations and experiments as well as possible in terms of five pieces of information for each cooling stage, namely the concentration profile over time, and the average sizes and variances (in both L_1 and L_2 directions) of the final PSSD (note all simulations have been started with an ensemble of crystals having exactly the same PSSD as that measured). The estimated parameters are reported in Table 8, together with their 95% confidence intervals. The simulated results are shown in Figs. 10 and 11 together with the experimental measurements for the sake of comparison: simulated dark blue concentration profiles are plotted in Fig. 10; red squares represent the final $L_{1,N}$ and $\sigma_{1,N}$ in the upper and lower panel, respectively, of Fig. 10; the red contour lines in the lower part of Fig. 11 illustrate the simulated final PSSDs for experiments Exp 1 and Exp 2.

While we are fully aware that the agreement between simulations and measurements is not perfect, we would argue that it is reasonably good (average absolute error of 15 µm for L_1 and 5 µm for L_2), since all main trends are properly captured. More specifically, we consider the estimated growth rates as sufficient to provide a reasonable estimate of the ratio G_1/G_2, whose importance in the context of the 3-stage process has been demonstrated above. Considering the size dependence of G_1 and assuming L_1 varying between 100 µm and 300 µm yield a value of G_1/G_2 from Eqs. (17) and (18) between about 15 and about 40. This is a much larger value than in the case of β L-Glutamic acid, which leads to the conjecture that the γ D-Mannitol system behaves similar to the system in the bottom left corner of Fig. 1, i.e. a system characterized by a large value of both G_1/G_2 and D_1/D_2.

4.2. From attainable region to process design

Based on the type of attainable region obtained, it is possible to heuristically optimize the operating conditions that should eventually be applied when the 3-stage process is implemented.

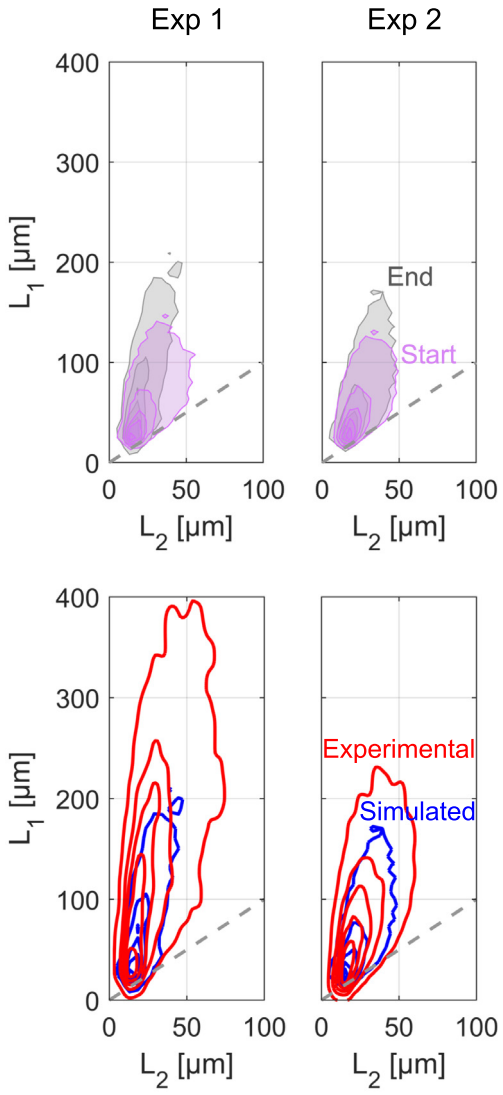

Fig. 11. In the first row, the particle size and shape distributions collected at the beginning (pink) and at the end (gray) of two cooling stages are shown, highlighting the increased broadness of the final PSSD in comparison to the original one. On the second row, a comparison between the PSSD at the end of the cooling stage, both measured (blue) and simulated (red), is carried out, showing the agreement between model and experiments.

Table 8
Estimated values of the kinetic parameters and their 95% confidence intervals.

Parameter	Estimated value
p_{11} $[\frac{\mu m}{s}]$	30.2 ± 1.5
p_{14} $[-]$	0.81 ± 0.04
p_{21} $[\frac{\mu m}{s}]$	0.20 ± 0.03

In the case of low G_1/G_2 and high D_1/D_2 ratios (bottom right corner of Fig. 1), as in the case of β L-Glutamic acid, the process can actually lead to a wide variety of sizes and shapes. As shown elsewhere (Salvatori and Mazzotti, 2017, 2018a), a good compromise between the improved crystal morphology and the productivity of the process is represented by heuristically optimal conditions, where a moderate milling intensity is combined with a large number of cycles.

On the other hand, for high G_1/G_2 and low D_1/D_2 ratios (top left corner of Fig. 1), the best operating conditions correspond to the minimum number of cycles and the highest milling intensity. This choice provides a compromise between productivity, number of fines in the product, and morphology of the crystals at the end of the process.

For situations similar to the case of γ D-Mannitol, the heuristically optimal operating conditions correspond to a high milling intensity, with the aim of improving particle morphology, and an intermediate (3–4) number of cycles, to remove the fines formed during breakage.

It is important to notice that the strategy proposed is based only on the outcome of the four factorial experiments and does not require any mathematical model, thus reducing the characterization effort to a minimum.

4.3. Exploration of the process design space

The attainable regions shown for γ D-Mannitol and β L-Glutamic acid have been obtained by varying the rotor speed and the number of cycles. It is clear that this covers only a subset of the whole design space characteristic of the 3-stage process and is therefore necessary to understand if and how varying the other operating conditions can change the type of attainable region obtained.

In particular, another operating parameter that can be varied is the fraction of mass dissolved (Salvatori and Mazzotti, 2017, 2018a). In order to investigate its effect on the attainable region for different compounds, some considerations can be made based on the compound-specific properties, as well as on the simulation results. We start by analyzing the case of large D_1/D_2 and small G_1/G_2 ratios (bottom right corner of Fig. 1). For this type of compounds, increasing the fraction of mass dissolved has a beneficial effect, since more crystal mass would be removed during dissolution, making the particles shorter, and solute would be recovered during cooling by growth along L_2, thus obtaining more compact crystals (see panel (b) of Fig. 2). In this case, the shape of the attainable region does not change, but different sizes can be achieved. The same situation occurs for compounds with small D_1/D_2 and large G_1/G_2 ratios (top left corner of Fig. 1).

Less intuitive are the two remaining cases, that is compounds with small (large) D_1/D_2 and small (large) G_1/G_2 ratios, for which the model can indeed be used to gain a better insight. Fig. 12 shows the effect of increasing the fraction of mass dissolved for two of these intermediate cases. It is readily observed that changing this operating condition does indeed change the shape of the attainable region, but leads to product particles with a worse morphology. Further, increasing the fraction of mass dissolved leads to particles with a more equant shape only if the change in length L_1 of the crystals during the crystallization step is smaller than its reduction during the dissolution stage.

For a more in-depth investigation of the effect of changing the mass dissolved during the heating steps on the PSSD of the product crystals, one can use the model that we have developed in Section 4.1.4 for γ D-Mannitol. Such model would be applied beyond the scope of the experiments used to estimate its model parameters, namely to study the effect of changing m_D based on fitting experiments carried out all with the same value of m_D. In order to check whether this is possible, we have carried out one 3-stage process experiment under the same conditions as run M5 in Table 7, but with 50% of mass dissolved during the dissolution stages instead of 20% only. The results of such experiments are illustrated in Fig. 13, where the left-hand side shows the initial (pink contour lines and shade) and final (gray) PSSDs measured with the μ-DISCO and the right-hand side shows the measured (blue) and the calculated (red) final PSSDs. It is readily observed that the agreement between simulation result and experimental

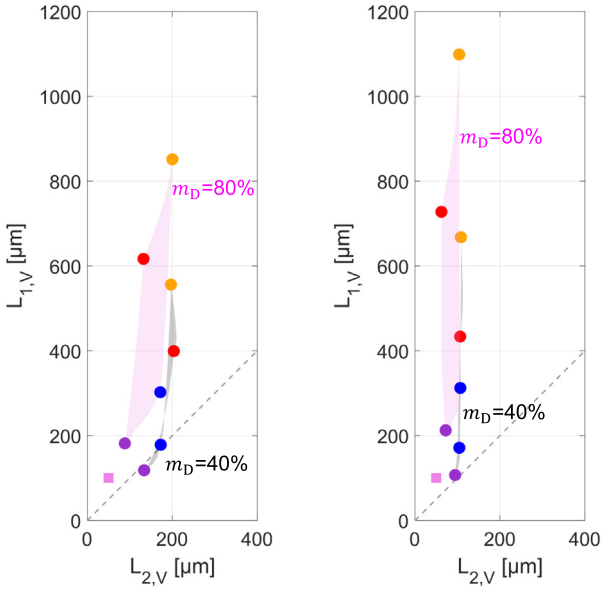

Fig. 12. Simulations aimed at investigating the effect of the fraction mass dissolved on the attainable region of the 3-stage process (left panel: $G_1/G_2 = 1.5$ and $D_1/D_2 = 0.2$; right panel: $G_1/G_2 = 12$ and $D_1/D_2 = 1.9$).

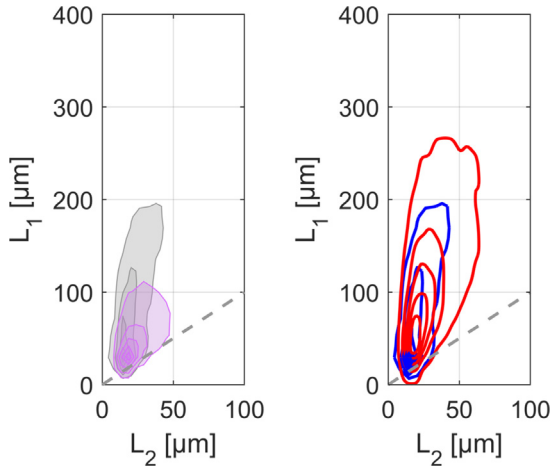

Fig. 13. Results of the experiment performed adopting the operating conditions reported in Tables 6 and 7 for experiment M5 dissolving 50% of the mass suspended. In the left panel, the particle size and shape distributions collected at the beginning (pink) and at the end (gray) of two cooling stages are shown. In the right panel, the comparison between simulation (red) and experimental (blue) results is reported. (For interpretation of the references to color in this figure legend, the reader is referred to the web version of this article.)

measure is acceptable, i.e. similar to the error observed in the case of the cooling experiments used to estimate the growth model parameters. We consider this result very encouraging, because it demonstrates the possibility of efficiently exploring the design space of the 3-stage process.

5. Conclusions

The 3-stage process certainly represents a valid approach to manipulate the size and shape of crystals, but its shortcomings, particularly concerning the very broad design space and its characterization when applied to different compounds, question its applicability. In this work we tacked these problems by developing a robust and effective approach to characterize the 3-stage process feasibility and potential for different compounds with a contained characterization effort.

First, we used the model to determine generally valid compound-dependent features. In particular, the attainable region, which is the portion of the L_1L_2-plane corresponding to all the possible process outcomes, has been identified through process simulations performed with different growth and dissolution kinetics. This analysis allowed to pinpoint, as key characteristics of the system, the growth and dissolution rates ratios, which strongly affect the type and shape of the attainable region. These simulations were used to define a small set of experiments to fully identify the attainable region without performing a comprehensive and time demanding process characterization.

The strategy developed has therefore been applied to experimentally investigate the outcome of the 3-stage process when applied to two different compounds, namely β L-Glutamic acid and γ D-Mannitol. The results validated the observation obtained through simulations and confirmed the developed model-free approach as a valid tool for an efficient process characterization. We then used the experimental data acquired throughout the factorial experiments to estimate the growth kinetics of γ D-Mannitol and compare the behavior of both model compounds.

The experiments have been combined with the information acquired via process simulations in order to define, for each type of attainable region, heuristic optimal conditions granting the best compromise between productivity and crystal shape. Finally, the experimental data are used to tune the model parameters and run simulations to explore the whole design space and predict the properties of the 3-stage process products.

The main strength of the proposed approach lies in its general validity, as it is not necessary to fully characterize the system to quantify the outcome of the 3-stage process, but only a limited set of tests, namely the four factorial experiments, can be used to this aim. This is particularly interesting given the reduced amount of material and effort required to carry out the tests. Analyzing different compounds also allowed to experimentally observe the different attainable region obtained via simulations. Based on the type of attainable region, general heuristic optimal conditions have been defined, which are mainly based on common properties of the final size and shape of the crystals and not on the specific features of the system. This is of great relevance, as it is possible to apply the identified conditions merely according to the type of attainable region obtained, thus saving a time demanding process optimization for each compound investigated. Furthermore, gaining access to the information throughout each stage showed how a deeper insight in different aspects of the 3-stage process and the system can be achieved without further characterization effort, especially when this information is combined with the model. In this case, the effect of different operating conditions, once the kinetics of the system have been estimated, can be investigated in silico, thus leading to the possibility of greatly enlarging and exploring the process design space without performing time-consuming and expensive experiments, a possibility certainly valuable for research and development purposes.

Conflict of interest

The authors declared that there is no conflict of interest.

Acknowledgements

The authors thank F. Hoffmann–La Roche AG for the support in the course of this project, as well as Stefan Bötschi and Ashwin Kumar Rajagopalan, ETH Zurich, for the fruitful discussions.

Appendix A

A.1. MPBE for the crystallization stage

The MPBE for a well stirred batch crystallizer, where no breakage and no agglomeration occur, reads as follows:

$$\frac{\partial n}{\partial t}+\frac{\partial(G_1 n)}{\partial L_1}+\frac{\partial(G_2 n)}{\partial L_2}=J_N\delta(L_1)\delta(L_2) \tag{19}$$

$$n(L_1,L_2,t=0)=n_{0,C}(L_1,L_2) \tag{20}$$

$$n(L_1=0,L_2,t)=0 \tag{21}$$

$$n(L_1,L_2=0,t)=0 \tag{22}$$

Here, G_1 and G_2 represent the growth rates along the internal coordinates L_1 and L_2, while the term $J\delta(L_1)\delta(L_2)$ represents the formation of new crystals of size $L_1=L_2=0$ due to nucleation events. Eq. (20) is the initial condition for Eq. (19), whereas Eqs. (21) and (22) are its boundary conditions; $n_{0,C}(L_1,L_2)$ represents the particle size and shape distribution of crystals at the beginning of the cooling stage.

Eq. (19) is coupled with a mass balance for the solute concentration in the liquid phase, c, which under the assumption of constant mass of solvent reads as

$$\frac{\mathrm{d}c}{\mathrm{d}t}=-k_V\rho\frac{\mathrm{d}\mu_{12}}{\mathrm{d}t} \tag{23}$$

$$c(t=0)=c_0 \tag{24}$$

Here, k_V is the shape factor, equal to $\pi/4$ for cylinders, and μ_{12} is one of the moments of the particle size and shape distribution, which is directly proportional to the mass of crystals suspended per unit mass of solvent and is defined as

$$\mu_{12}(t)=\int_0^\infty\int_0^\infty n(L_1,L_2,t)L_1L_2^2\mathrm{d}L_1\mathrm{d}L_2 \tag{25}$$

The supersaturation S, in the case of either mild non-idealities or negligible effect of the composition on the activity coefficient of the solute, can be defined as the ratio between the concentration of solute in solution and its solubility at the temperature T:

$$S=\frac{c}{c^*(T)} \tag{26}$$

The constitutive equations for growth and nucleation, both primary and secondary, have been adapted from Ochsenbein et al. (2014) and Ploss and Mersmann (1989), and derived from the classical nucleation theory.

$$G_i=k_{G,i1}\exp\left(-\frac{k_{G,i2}}{T}\right)(S-1)^{k_{G,i3}}\quad\text{with } S>1 \tag{27}$$

$$J_N=J_S+J_{He}+J_{Ho} \tag{28}$$

$$J_S=k_{S,1}\varepsilon^{k_{S,2}}m_S^{k_{S,3}}\overline{G}^{k_{S,4}} \tag{29}$$

$$J_{Ho}=k_{Ho,1}\exp\left(-\frac{k_{Ho,2}}{\ln^2 S}\right) \tag{30}$$

$$J_{He}=k_{He,1}\exp\left(-\frac{k_{He,2}}{\ln^2 S}\right) \tag{31}$$

Here, ε is the power input, m_S the suspension density, $\overline{G}$ is the average growth rate, calculated as $(G_1+G_2)/2$.

A.2. MPBE for the milling stage

The MPBE for a continuous rotor-stator wet mill, under the assumption of perfectly segregated flow (i.e.the grinding chamber is assumed to be a tubular apparatus), constant supersaturation, and isothermal conditions, reads as (Salvatori and Mazzotti, 2018b):

$$\frac{\partial n(L_1,L_2,\tau)}{\partial\tau}=B_1+B_2-D \tag{32}$$

$$B_1=\int_{L_1}^\infty K_1(x,L_2)n(x,L_2,\tau)g_1(L_1,x)\mathrm{d}x \tag{33}$$

$$B_2=\int_{L_2}^\infty K_2(L_1,x)n(L_1,x,\tau)g_2(L_2,x)\mathrm{d}x \tag{34}$$

$$D=K_1(L_1,L_2)n(L_1,L_2,\tau)+K_2(L_1,L_2)n(L_1,L_2,\tau) \tag{35}$$

$$n(L_1,L_2,\tau=0)=n_{0,M}(L_1,L_2) \tag{36}$$

The functions K_i and $g_i(L_i,x)$ are called breakage frequency and daughter distribution respectively and are used to model how fast the particles break along the relevant direction and the size of the fragments formed, according to the type of mechanism underlying the breakage events. The functional forms adopted in this work are:

$$K_1=k_{M,11}m_M(\theta r_M)^2\left(\frac{L_1}{L_{ref,1}}\right)^{k_{M,12}}\left(1+\exp\left(-\frac{L_1-k_{M,13}}{L_{ref,2}}\right)\right)^{-1}\frac{\Phi}{\Phi+k_{M,14}} \tag{37}$$

$$K_2=k_{M,21}m_M(\theta r_M)^2\left(\frac{L_2}{L_{ref,1}}\right)^{k_{M,22}}\left(1+\exp\left(-\frac{L_2-k_{M,23}}{L_{ref,2}}\right)\right)^{-1}\frac{k_{M,24}}{k_{M,24}+\Phi} \tag{38}$$

$$g_1(L_1,x)=\frac{2}{x} \tag{39}$$

$$g_2(L_2,x)=\frac{4L_2}{x^2} \tag{40}$$

In our previous paper (Salvatori and Mazzotti, 2018b) this model has been developed and verified for the same type of device and operations exploited in this work.

A.3. MPBE for the dissolution stage

The MPBE for the batch, well-mixed dissolution stage is similar to that presented for the crystallization stage:

$$\frac{\partial n}{\partial t}+\frac{\partial(D_1 n)}{\partial L_1}+\frac{\partial(D_2 n)}{\partial L_2}=0 \tag{41}$$

$$n(L_1,L_2,t=0)=n_{0,D}(L_1,L_2) \tag{42}$$

$$n(L_1=0,L_2,t)=0 \tag{43}$$

$$n(L_1,L_2=0,t)=0 \tag{44}$$

Here, D_i is the dissolution rate along characteristic dimension L_i and has a negative value. The material balance of Eq. (23) is coupled with Eq. (41) to ensure conservation of mass. The functional form chosen is that proposed by Eisenschmidt et al. (2015).

$$D_i=-k_{D,i1}\exp\left(-\frac{k_{D,i2}}{T}\right)(1-S)^{k_{D,i3}}\quad\text{with } S<1 \tag{45}$$

References

Agimelen, O.S., Svoboda, V., Ahmed, B., Cardona, J., Dziewierz, J., Brown, C.J., McGlone, T., Cleary, A., Tachtatzis, C., Michie, C., Florence, A.J., Andonovic, I., Mulholland, A.J., Sefcik, J., 2018. Multi-sensor inline measurements of crystal size and shape distributions during high shear wet milling of crystal slurries. Adv. Powder Technol., 1–9

Bakalis, S., Le Révérend, B.J., Anwar, N.Z.R., Fryer, P.J., 2011. Modelling crystal polymorphisms in chocolate processing. Proc. Food Sci. 1, 340–346.

Borchert, C., Sundmacher, K., 2012. Morphology evolution of crystal populations: modeling and observation analysis. Chem. Eng. Sci. 70, 87–98.

Chatterjee, A., Gupta, M.M., Birendra, S., 2017. Spherical crystallization: a technique use to reform solubility and flow property of active pharmaceutical ingredients. Int. J. Pharm. Invest. 7, 4–9.

Chemburkar, S.R. et al., 2000. Dealing with the impact of ritonavir polymorphs on the late stages of bulk drug process development. Org. Process Res. Dev. 4, 413–417.

Cornel, J., Lindenberg, C., Mazzotti, M., 2009. Experimental characterization and population balance modeling of the polymorph transformation of L-Glutamic Acid. Cryst. Growth Des. 9, 243–252.
Cornel, J., Kidambi, P., Mazzotti, M., 2010. Precipitation and transformation of the three polymorphs of d-mannitol. Ind. Eng. Chem. Res. 49, 5854–5862.
Eisenschmidt, H., Voigt, A., Sundmacher, K., 2015. Face-specific growth and dissolution kinetics of potassium dihydrogen phosphate crystals from batch crystallization experiments. Cryst. Growth Des. 15, 219–227.
Gordon, M.S., 1994. Process considerations in reducing tablet friability and their effect on in vitro dissolution. Drug Dev. Ind. Pharm. 20, 11–29.
Gunawan, R., Fusman, I., Braatz, R.D., 2004. High resolution algorithms for multidimensional population balance equations. AIChE J. 50, 2738–2749.
Gupta, M.K., Vanwert, A., Bogner, R.H., 2003. Formation of physically stable amorphous drugs by milling with Neusilin. J. Pharm. Sci. 92, 536–551.
Heng, J.Y.Y., Thielmann, F., Williams, D.R., 2006. The effects of milling on the surface properties of form I paracetamol crystals. Pharm. Res. 23, 1918–1927.
Kempkes, M., Vetter, T., Mazzotti, M., 2010. Measurement of 3D particle size distributions by stereoscopic imaging. Chem. Eng. Sci. 65, 1362–1373.
Khadka, P., Ro, J., Kim, H., Kim, I., Kim, J.T., Kim, H., Cho, J.M., Yun, G., Lee, J., 2014. Pharmaceutical particle technologies: an approach to improve drug solubility, dissolution and bioavailability. Asian J. Pharm. Sci. 9, 304–316.
Klapwijk, A.R., Simone, E., Nagy, Z.K., Wilson, C.C., 2016. Tuning crystal morphology of succinic acid using a polymer additive. Cryst. Growth Des. 16, 4349–4359.
Kumar, S., Ramkrishna, D., 1996. On the solution of population balance equations by discretization – I. A fixed pivot technique. Chem. Eng. Sci. 51, 1311–1332.
Lin, S.Y., Hsu, C.H., Ke, W.T., 2010. Solid-state transformation of different gabapentin polymorphs upon milling and co-milling. Int. J. Pharm. 396, 83–90.
Liversidge, G.G., Cundy, K.C., 1995. Particle size reduction for improvement of oral bioavailability of hydrophobic drugs: I. Absolute oral bioavailability of nanocrystalline danazol in beagle dogs. Int. J. Pharm. 125, 91–97.
Lovette, M.A., Muratore, M., Doherty, M.F., 2012. Crystal shape modification through cycles of dissolution and growth: attainable regions and experimental validation. AIChE J. 58, 1465–1474.
Nokhodchi, A., Amire, O., Jelvehgari, M., 2010. Physico-mechanical and dissolution behaviours of ibuprofen crystals crystallized in the presence of various additives. Tehran Univ. Med. Sci. 18, 74–83.
Ochsenbein, D.R., Schorsch, S., Vetter, T., Mazzotti, M., Morari, M., 2014. Growth rate estimation of β L-glutamic acid from online measurements of multidimensional particle size distributions and concentration. Ind. Eng. Chem. Res. 53, 9136–9148.
Ploss, R., Mersmann, A., 1989. A new model of the effect of stirring intensity on the rate of secondary nucleation. Chem. Eng. Technol. 12, 137–146.
Powell, K.A., Saleemi, A.N., Rielly, C.D., Nagy, Z.K., 2016. Monitoring continuous crystallization of paracetamol in the presence of an additive using an integrated PAT array and multivariate methods. Org. Process Res. Dev. 20, 626–636.
Rajagopalan, A.K., Schneeberger, J., Salvatori, F., Bötschi, S., Ochsenbein, D.R., Oswald, M.R., Pollefeys, M., Mazzotti, M., 2017. A comprehensive shape analysis pipeline for stereoscopic measurements of particulate populations in suspension. Powder Technol. 321, 479–493.
Ramkrishna, D., 2000. Population Balances: Theory and Applications to Particulate Systems in Engineering. Academic Press, p. 355.
Salvalaglio, M., Vetter, T., Mazzotti, M., Parrinello, M., 2013. Controlling and predicting crystal shapes: the case of urea. Angew. Chem. – Int. Ed. 52, 13369–13372.
Salvatori, F., Mazzotti, M., 2017. Manipulation of particle morphology by crystallization, milling, and heating cycles – a mathematical modeling approach. Ind. Eng. Chem. Res. 56, 9188–9201.
Salvatori, F., Mazzotti, M., 2018a. Manipulation of particle morphology by crystallization, milling, and heating cycles: experimental characterization. Ind. Eng. Chem. Res. 57, 15522–15533.
Salvatori, F., Mazzotti, M., 2018b. Experimental characterization and mathematical modeling of breakage of needle-like crystals in a continuous rotor-stator wet mill. Cryst. Growth Des. 18, 5957–5972.
Schöll, J., Bonalumi, D., Vicum, L., Mazzotti, M., Müller, M., 2006. In situ monitoring and modeling of the solvent-mediated polymorphic transformation of L-glutamic acid 2006. Cryst. Growth Des. 6, 881–891.
Schorsch, S., Vetter, T., Mazzotti, M., 2012. Measuring multidimensional particle size distributions during crystallization. Chem. Eng. Sci. 77, 130–142.
Shangwal, K., 2007. Additives and Crystallization Processes: From Fundamentals to Applications. John Wiley & Sons.
Simone, E., Steele, G., Nagy, Z.K., 2015. Tailoring crystal shape and polymorphism using combinations of solvents and a structurally related additive. CrystEngComm 17, 9370–9379.
Simone, E., Klapwijk, A.R., Wilson, C.C., Nagy, Z.K., 2017. Investigation of the evolution of crystal size and shape during temperature cycling and in the presence of a polymeric additive using combined process analytical technologies. Cryst. Growth Des. 17, 1695–1706.
Singhal, D., Curatolo, W., 2004. Drug polymorphism and dosage form design: a practical perspective. Adv. Drug Deliv. Rev. 56, 335–347.
Singh, M.R., Chakraborty, J., Nere, N., Tung, H.H., Bordawekar, S., Ramkrishna, D., 2012. Image-analysis-based method for 3D crystal morphology measurement and polymorph identification using confocal microscopy. Cryst. Growth Des. 12, 3735–3748.
Sun, C.C., 2011. Decoding powder tabletability: roles of particle adhesion and plasticity. J. Adhes. Sci. Technol. 25, 483–499.
Sun, C., Grant, D.J.W., 2001. Influence of crystal shape on the tableting performance of L-Lysine monohydrochloride dihydrate. Pharmacia 90, 569–579.
Taborga, P., Brito, I., Graber, T.A., 2017. Effect of additives on size and shape of lithium carbonate crystals. J. Cryst. Growth 460, 5–12.
Tien, C., Bai, R., Ramarao, B.V., 1996. Analysis of effect cake growth in of fine particle cake filtration: retention. AIChE J. 43, 33–44.
van Antwerpen, F., van Krevelen, D.W., 1972. Influence of crystallization temperature, molecular weight, and additives on the crystallization kinetics of poly(ethylene terephtalate). J. Polym. Sci. Polym. Phys. Ed. 10, 2423–2435.
Wan, J., Wang, X.Z., Ma, C.Y., 2009. Particle shape manipulation and optimization in cooling crystallization involving multiplecrystal morphological forms. AIChE J. 55, 2049–2061.